




## Spin-valley locking in Kekulé-distorted graphene with Dirac-Rashba interactions

David A. Ruiz-Tijerina <sup>1,\*</sup>, Jesús Arturo Sánchez-Sánchez,<sup>2,3</sup> Ramon Carrillo-Bastos <sup>4</sup>,  
Santiago Galván y García,<sup>2,3</sup> and Francisco Mireles <sup>2,†</sup>

<sup>1</sup>*Departamento de Física Química, Instituto de Física, Universidad Nacional Autónoma de México, Ciudad de México, C.P. 04510, Mexico*

<sup>2</sup>*Departamento de Física, Centro de Nanociencias y Nanotecnología, Universidad Nacional Autónoma de México, Apartado Postal 14, 22800 Ensenada, Baja California, Mexico*

<sup>3</sup>*Instituto de Ciencias Físicas, Universidad Nacional Autónoma de México, Cuernavaca, Morelos, 62210, Mexico*

<sup>4</sup>*Facultad de Ciencias, Universidad Autónoma de Baja California, Apartado Postal 1880, 22800 Ensenada, Baja California, Mexico*



(Received 4 August 2023; revised 9 December 2023; accepted 18 January 2024; published 9 February 2024)

The joint effects of Kekulé lattice distortions and Rashba-type spin-orbit coupling on the electronic properties of graphene are explored. We modeled the position dependence of the Rashba energy term in a manner that allows its seamless integration into the scheme introduced by Gamayun *et al.* [*New J. Phys.* **20**, 023016 (2018)] to describe graphene with Kekulé lattice distortion. Particularly for the Kekulé-Y (Kek-Y) texture, the effective low-energy Dirac Hamiltonian contains a new spin-valley locking term in addition to the well-known Rashba-induced momentum-pseudospin and spin-pseudospin couplings and the Kekulé-induced momentum-valley coupling term. We report on the low-energy band structure and Landau level spectra of Rashba-spin-orbit-coupled Kek-Y graphene and propose an experimental scheme to discern between the presence of Rashba spin-orbit coupling, Kek-Y lattice distortion, and both based on doping-dependent magnetotransport measurements.

DOI: [10.1103/PhysRevB.109.075410](https://doi.org/10.1103/PhysRevB.109.075410)

### I. INTRODUCTION

In recent years, graphene-metal hybrid systems have attracted much attention because they showcase new and exciting electronic and magnetic phenomena not present in pristine graphene [1]. Through proximity effects, these hybrid systems enable the modification and control of the electronic properties of pristine graphene, such as opening a gap between the valence and conduction bands [2]; distorting the linear behavior of carriers at low energies [3]; and introducing the anomalous, spin, and spin-quantum Hall effects [4–6]. Researchers aim to break graphene’s symmetries—from which many of its extraordinary properties originate—through various mechanisms to turn graphene into a suitable candidate for spintronic applications [7]. Two of the most actively researched mechanisms for breaking graphene’s symmetries are lattice deformations and spin-orbit effects induced by proximity [8–13]. Throughout this paper, we shall focus on these two mechanisms, combining specifically Kekulé lattice distortions and proximity-induced Rashba spin-orbit (RSO) coupling.

On the one hand, a Kekulé Y-shaped bond pattern (Kek-Y) was experimentally obtained in 2016 by Gutierrez *et al.* [14,15] by growing graphene epitaxially on a Cu(111) surface and was attributed to the commensurate lattice constants of graphene and the copper substrate, combined with the presence of copper vacancies acting as “ghost” adatoms. Eom and Koo [16] observed both Kek-Y and Kek-O textures by inducing nanoscale strain on graphene using a silicon

dioxide substrate. Finally, the graphene Kek-O texture was observed by Li *et al.* in quantum Hall ferromagnetic states [17] and, more recently, by Bao *et al.* in Li-intercalated graphene samples [18,19] and by Qu *et al.* in graphene decorated with Li adatoms [20]. In order to determine the electronic structure of graphene with Kekulé lattice distortion, Gamayun *et al.* [21] derived low-energy Dirac Hamiltonians for both the Kek-Y and Kek-O textures. In the former case, they found that the lattice distortion introduces a new coupling between the electronic momentum and its valley isospin as a result of the broken chiral symmetry. The low-energy spectrum preserved its linear behavior near the Fermi level, but with the valley degeneracy breaking resulting in two Dirac bands with distinct Fermi velocities.

On the other hand, Rashba-type spin-orbit coupling has been confirmed in graphene due to proximity effects with metallic substrates. This extrinsic effect is momentum independent in the single-valley approximation and causes an energy splitting between opposite spin states of 13–225 meV [22–25]: 3 to 4 orders of magnitude greater than the splitting associated with graphene’s intrinsic spin-orbit coupling [26–28]. Such a substantial enhancement of the RSO interaction has been mainly attributed to hybridization between carbon’s  $2p_z$  orbitals and the metal substrate’s  $d$  orbitals and broken lattice symmetry in graphene [29]. Moreover, the RSO interaction strength has been shown to be tunable via external gate voltages, as well as local lattice deformations [11,30]. Given the bond length dependence of the Rashba parameter [30], the following question naturally arises: How will the RSO coupling be modified by the presence of Kekulé lattice distortions in graphene? In this paper, we aim to answer this question. We introduce a generalized tight-binding

\*d.ruiz-tijerina@fisica.unam.mx

†fmireles@ens.cnyn.unam.mx

Hamiltonian for graphene with RSO coupling and Kekulé lattice distortion, parametrized via position-dependent hopping and spin-orbit interaction terms, exhibiting Kekulé periodicity. After mapping the problem onto reciprocal space and folding the graphene bands onto the Kekulé Brillouin zone (KBZ), we derive effective  $\mathbf{k} \cdot \mathbf{p}$ -type Hamiltonians for both the Kek-Y and Kek-O textures that are valid for the bands nearest the Fermi level. We then use these effective Hamiltonians to compute the low-energy band spectra of Kekulé distorted graphene with RSO coupling and discuss its most salient features, including the resulting spin, pseudospin, and valley textures. Finally, we introduce an out-of-plane magnetic field in the minimal coupling approximation [31] for the Kek-Y case and compute its Landau level (LL) spectrum, focusing on the competing effects of the Kekulé and RSO terms in magnetotransport. In particular, we identify different trends for the horizontal LL splittings in a carrier density vs magnetic field diagram in the cases of graphene with only a Kek-Y distortion, graphene with only RSO coupling, and graphene with both a Kek-Y distortion and RSO coupling. We propose that these distinct trends may be used to experimentally identify the presence of Kek-Y distortions, RSO coupling, or both on graphene-metal hybrid structures.

## II. TIGHT-BINDING MODEL

### A. Tight-binding model

The tight-binding Hamiltonian for a single layer of graphene with proximity-induced, sublattice-resolved Dirac-Rashba spin-orbit coupling [6,32] and a Kekulé lattice distortion [21] can be written as  $H^{pq} = H_0^{pq} + H_R^{pq}$ , with the spinless graphene Hamiltonian

$$H_0^{pq} = - \sum_{\mu} \sum_{\mathbf{R}} \sum_{j=1}^3 (t_{\mathbf{R},\mathbf{R}+\delta_j}^{pq} a_{\mathbf{R},\mu}^{\dagger} b_{\mathbf{R}+\delta_j,\mu} + \text{H.c.}), \quad (1)$$

where  $a_{\mathbf{R},\mu}^{\dagger}$  ( $a_{\mathbf{R},\mu}$ ) is the creation (annihilation) operator for an electron on site  $\mathbf{R}$  of sublattice  $A$ , with spin projection  $\mu = \uparrow, \downarrow$ , and  $b_{\mathbf{R}+\delta_j,\mu}^{\dagger}$  ( $b_{\mathbf{R}+\delta_j,\mu}$ ) are the corresponding  $B$  sublattice operators. The integers  $p$  and  $q$  parametrize the Kekulé bond texture over the honeycomb lattice, as shown below [see Eqs. (2) and (7)]. In the case of pristine graphene ( $\Delta = 0$ ), each atom at site  $\mathbf{R}$  is connected to three nearest neighbors at sites  $\mathbf{R} + \delta_j$ , with relative position vectors  $\delta_1 = \frac{a_0}{2}(\sqrt{3}, -1)$ ,  $\delta_2 = -\frac{a_0}{2}(\sqrt{3}, 1)$ , and  $\delta_3 = a_0(0, 1)$ , where  $a_0 = 1.421 \text{ \AA}$  is the unperturbed C-C bond length. The lattice vectors are  $\mathbf{a}_1 = \delta_3 - \delta_1$  and  $\mathbf{a}_2 = \delta_3 - \delta_2$ . However, the presence of a Kekulé bond distortion will modulate the

hopping terms  $t_{\mathbf{R},\mathbf{R}+\delta_j}^{pq}$  as [21]

$$\frac{t_{\mathbf{R},\mathbf{R}+\delta_j}^{pq}}{t_0} = 1 + 2\text{Re}[\Delta e^{i\mathbf{K}_{pq} \cdot \delta_j + i\mathbf{G} \cdot \mathbf{R}}]. \quad (2)$$

Here,  $\mathbf{K}_{pq} \equiv p\mathbf{K}_+ + q\mathbf{K}_-$ , with the graphene valley vectors

$$\mathbf{K}_{\pm} = \frac{4\pi}{3\sqrt{3}a_0} \left( \pm \frac{1}{2}, \frac{\sqrt{3}}{2} \right), \quad (3)$$

and the vector

$$\mathbf{G} \equiv \mathbf{K}_+ - \mathbf{K}_- = \frac{4\pi}{3\sqrt{3}a_0} (1, 0) \quad (4)$$

is a Kekulé superlattice primitive Bragg vector. The type of bond texture is determined by the integer ( $\in \mathbb{Z}_3$ )

$$n = (1 + q - p) \bmod 3, \quad (5)$$

where a Kek-O texture corresponds to  $n = 0$ , whereas Kek-Y textures are obtained for  $n = \pm 1$ .

Since  $\mathbf{G}$  connects the two graphene valleys  $\mathbf{K}_{\pm}$  in reciprocal space, the latter are folded down onto the  $\Gamma$  point of the KBZ. The hopping term modulation amplitude  $\Delta$  is, in general, complex valued, although in the remainder of this paper we shall take both  $\Delta$  and  $t$  to be real without loss of generality. Finally, we point out that, for pristine graphene, the nearest-neighbor hopping integral reduces to  $t_0 = 3.16 \text{ eV}$ .

The Dirac-Rashba spin-orbit term has the form

$$H_R^{pq} = \sum_{\mu\nu} \sum_{\mathbf{R}} \sum_{j=1}^3 \left[ \frac{i\lambda_{\mathbf{R},\mathbf{R}+\delta_j}^{pq}}{2} a_{\mathbf{R},\mu}^{\dagger} (\mathbf{s}_{\mu\nu} \times \hat{\delta}_j)_z b_{\mathbf{R}+\delta_j,\nu} - \text{H.c.} \right], \quad (6)$$

where  $\mathbf{s}$  is the vector of Pauli matrices acting on the physical spin subspace, whereas  $\hat{\delta}_j = \delta_j/|\delta_j|$ . We have allowed a periodic bond length modulation of the Rashba spin-orbit coupling  $\lambda_{\mathbf{R},\mathbf{R}+\delta_j}^{pq}$ , analogous to that of the hopping parameter in Eq. (2), with a complex amplitude  $\xi$ :

$$\frac{\lambda_{\mathbf{R},\mathbf{R}+\delta_j}^{pq}}{\lambda_R} = 1 + 2\text{Re}[\xi e^{i\mathbf{K}_{pq} \cdot \delta_j + i\mathbf{G} \cdot \mathbf{R}}], \quad (7)$$

where  $\lambda_R$  is the Dirac-Rashba parameter in the absence of a Kekulé distortion.

Finally, we note that the Kekulé distortion also admits on-site energy modulation by ionic potentials [21] or by second-nearest-neighbor hopping [33]. These additional terms are discussed in Appendix E and will not be considered in our main discussion.

### B. Total Hamiltonian in reciprocal space

Taking the Fourier transforms of the total Hamiltonian gives the spin-conserving and Dirac-Rashba terms as

$$H_0^{pq} = \sum_{\mathbf{k} \in \text{BZ}} \sum_{\mu} [\Phi(\mathbf{k}) a_{\mathbf{k},\mu}^{\dagger} b_{\mathbf{k},\mu} + \Delta \Phi(\mathbf{k} + \mathbf{K}_{pq}) a_{\mathbf{k}+\mathbf{G},\mu}^{\dagger} b_{\mathbf{k},\mu} + \Delta \Phi(\mathbf{k} - \mathbf{K}_{pq}) a_{\mathbf{k}-\mathbf{G},\mu}^{\dagger} b_{\mathbf{k},\mu} + \text{H.c.}],$$

$$H_R^{pq} = i \sum_{\mathbf{k} \in \text{BZ}} \sum_{\mu,\nu} [a_{\mathbf{k},\mu}^{\dagger} \Lambda_{\mu\nu}(\mathbf{k}) b_{\mathbf{k},\nu} + \xi a_{\mathbf{k}+\mathbf{G},\mu}^{\dagger} \Lambda_{\mu\nu}(\mathbf{k} + \mathbf{K}_{pq}) b_{\mathbf{k},\nu} + \xi a_{\mathbf{k}-\mathbf{G},\mu}^{\dagger} \Lambda_{\mu\nu}(\mathbf{k} - \mathbf{K}_{pq}) b_{\mathbf{k},\nu} - \text{H.c.}], \quad (8)$$

with the sum over  $\mathbf{k}$  running over all wave vectors of the original (pristine graphene) Brillouin zone (BZ). We have also defined

$$\Phi(\mathbf{k}) = -t_0 \sum_{j=1}^3 e^{i\mathbf{k}\cdot\delta_j}, \quad \Lambda_{\mu\nu}(\mathbf{k}) = \frac{\lambda_R}{2} \sum_{j=1}^3 e^{i\mathbf{k}\cdot\delta_j} (\mathbf{s}_{\mu\nu} \times \hat{\delta}_j)_z. \quad (9)$$

We now perform a zone folding from the original BZ into the KBZ by introducing the 12-spinors  $\Psi_{\mathbf{k}} = (c_{\mathbf{k},\uparrow}, c_{\mathbf{k},\downarrow})^T$ , where

$$c_{\mathbf{k},\mu} = (a_{\mathbf{k},\mu}, a_{\mathbf{k}-\mathbf{G},\mu}, a_{\mathbf{k}+\mathbf{G},\mu}, b_{\mathbf{k}-\mathbf{G},\mu}, b_{\mathbf{k}+\mathbf{G},\mu}, b_{\mathbf{k},\mu})^T \quad (10)$$

and  $\mathbf{k} \in \text{KBZ}$ . Using the properties ( $m \in \mathbb{Z}$ )

$$\Xi(\mathbf{k}) = e^{i\frac{2\pi}{3}m} \Xi[\mathbf{k} + m(\mathbf{K}_+ + \mathbf{K}_-)] = \Xi(\mathbf{k} + 3m\mathbf{K}_{\pm}), \quad (11)$$

which are valid for both  $\Xi(\mathbf{k}) = \Phi(\mathbf{k})$  and  $\Xi(\mathbf{k}) = \Lambda(\mathbf{k})$ , we may write

$$H^{pq} = \sum_{\mathbf{k} \in \text{KBZ}} \Psi_{\mathbf{k}}^\dagger \mathcal{H}_{pq}(\mathbf{k}) \Psi_{\mathbf{k}}, \quad (12)$$

with the Bloch Hamiltonian

$$\mathcal{H}_{pq}(\mathbf{k}) = \begin{pmatrix} 0 & \mathcal{E}_n(\mathbf{k}) & 0 & i\mathcal{R}_n^{\uparrow\downarrow}(\mathbf{k}) \\ \mathcal{E}_n^{\dagger}(\mathbf{k}) & 0 & -i\mathcal{R}_n^{\downarrow\uparrow*}(\mathbf{k}) & 0 \\ 0 & i\mathcal{R}_n^{\downarrow\uparrow}(\mathbf{k}) & 0 & \mathcal{E}_n(\mathbf{k}) \\ -i\mathcal{R}_n^{\uparrow\downarrow*}(\mathbf{k}) & 0 & \mathcal{E}_n^{\dagger}(\mathbf{k}) & 0 \end{pmatrix} \quad (13)$$

containing the matrices

$$\mathcal{E}_n(\mathbf{k}) = \begin{pmatrix} \Phi_0(\mathbf{k}) & \Delta_{pq}\Phi_{n+1}(\mathbf{k}) & \Delta_{pq}^* \Phi_{-n-1}(\mathbf{k}) \\ \Delta_{pq}^* \Phi_{-n+1}(\mathbf{k}) & \Phi_{-1}(\mathbf{k}) & \Delta_{pq} \Phi_n(\mathbf{k}) \\ \Delta_{pq} \Phi_{n-1}(\mathbf{k}) & \Delta_{pq}^* \Phi_{-n}(\mathbf{k}) & \Phi_1(\mathbf{k}) \end{pmatrix},$$

$$\mathcal{R}_n^{\mu\nu}(\mathbf{k}) = \begin{pmatrix} \Lambda_0^{\mu\nu}(\mathbf{k}) & \xi_{pq}\Lambda_{n+1}^{\mu\nu}(\mathbf{k}) & \xi_{pq}^* \Lambda_{-n-1}^{\mu\nu}(\mathbf{k}) \\ \xi_{pq}^* \Lambda_{-n+1}^{\mu\nu}(\mathbf{k}) & \Lambda_{-1}^{\mu\nu}(\mathbf{k}) & \xi_{pq} \Lambda_n^{\mu\nu}(\mathbf{k}) \\ \xi_{pq} \Lambda_{n-1}^{\mu\nu}(\mathbf{k}) & \xi_{pq}^* \Lambda_{-n}^{\mu\nu}(\mathbf{k}) & \Lambda_1^{\mu\nu}(\mathbf{k}) \end{pmatrix}, \quad (14)$$

where we have introduced the folded tunneling function  $\Phi_n(\mathbf{k}) \equiv \Phi(\mathbf{k} + n\mathbf{G})$  and RSO coupling  $\Lambda_n^{\mu\nu}(\mathbf{k}) \equiv \Lambda_{\mu\nu}(\mathbf{k} + n\mathbf{G})$ , with  $n$  given by Eq. (5). We have also introduced the Kekulé terms

$$\Delta_{pq} \equiv e^{i\frac{2\pi}{3}(p+q)} \Delta, \quad \xi_{pq} \equiv e^{i\frac{2\pi}{3}(p+q)} \xi. \quad (15)$$

Note that all terms  $\Lambda_{\uparrow\uparrow}(\mathbf{k} + n\mathbf{G}) = \Lambda_{\downarrow\downarrow}(\mathbf{k} + n\mathbf{G}) = 0$ , by the symmetry of the Pauli matrices.

We may now obtain an effective low-energy model with reduced dimensionality  $8 \times 8$  by projecting out the two high-energy electron and hole bands present in  $\mathcal{H}_{pq}(\mathbf{k})$  for  $\mathbf{k}$  near the  $\Gamma$  point, corresponding to operators  $a_{\mathbf{k},\mu}$  and  $b_{\mathbf{k},\mu}$  in Eq. (10). We do so at zeroth order in perturbation theory and linearize  $\Phi_n(\mathbf{k})$  and  $\Lambda_n(\mathbf{k})$  about  $\mathbf{k} = \mathbf{0}$ . Finally, introducing the new 8-spinor basis

$$\Psi'_{\mathbf{k}} = (-b_{\mathbf{k}-\mathbf{G}\uparrow}, -b_{\mathbf{k}-\mathbf{G}\downarrow}, a_{\mathbf{k}-\mathbf{G}\uparrow}, a_{\mathbf{k}-\mathbf{G}\downarrow}, a_{\mathbf{k}+\mathbf{G}\uparrow}, a_{\mathbf{k}+\mathbf{G}\downarrow}, b_{\mathbf{k}+\mathbf{G}\uparrow}, b_{\mathbf{k}+\mathbf{G}\downarrow})^T, \quad (16)$$

we obtain two compact forms of  $\tilde{\mathcal{H}}_{pq}$  (Appendix A): All cases when  $(1+q-p) \bmod 3 = \pm 1$  give the Kek-Y Bloch

Hamiltonians

$$\mathcal{H}_Y(\mathbf{k}) = \hbar v_\sigma \tau_0(\mathbf{k} \cdot \boldsymbol{\sigma}) s_0 + \frac{\lambda_\sigma}{2} \tau_0(\boldsymbol{\sigma} \times \mathbf{s})_z + \hbar v_\tau (\mathbf{k} \cdot \boldsymbol{\tau}_\pm) \sigma_0 s_0 + \frac{\lambda_\tau}{2} (\boldsymbol{\tau}_\pm \times \sigma_0 \mathbf{s})_z, \quad (17)$$

whereas for  $(1+q-p) \bmod 3 = 0$  we obtain the Kek-O model

$$\mathcal{H}_O(\mathbf{k}) = \hbar v_\sigma \tau_0(\mathbf{k} \cdot \boldsymbol{\sigma}) s_0 + \frac{\lambda_\sigma}{2} \tau_0(\boldsymbol{\sigma} \times \mathbf{s})_z + 3t_0 \Delta \tau_x \sigma_z s_0. \quad (18)$$

Here, we use the standard definitions of the Pauli matrix vectors  $\boldsymbol{\sigma}$  and  $\mathbf{s}$  acting on the sublattice and spin degrees of freedom, respectively. For the valley subspace, we define the Pauli vectors  $\boldsymbol{\tau}_n = (n\tau_x, \tau_y, \tau_z)$ , where  $n = \pm 1$  corresponds to the type of Kek-Y texture defined by the parameters  $p$  and  $q$ .  $\tau_0$ ,  $\sigma_0$ , and  $s_0$  are the unit matrices in the valley, sublattice, and spin subspaces. We also define the two Fermi velocities  $v_\sigma = \frac{3}{2\hbar} t_0 a_0$  and  $v_\tau = \Delta v_\sigma$  and the constants  $\lambda_\sigma = \frac{3}{2} \lambda_R$  and  $\lambda_\tau = \xi \lambda_\sigma$ . The latter, introduced by the Kekulé-modulated RSO interaction in the Kek-Y case, constitutes a novel spin-valley coupling. By contrast, note that in a Kek-O texture there is no coupling between valley and momentum or valley and spin.

Both models  $\mathcal{H}_Y$  and  $\mathcal{H}_O$  can be diagonalized exactly, yielding the band structures

$$E_{\alpha,\beta,\gamma}^Y(\mathbf{k}) = \frac{\alpha}{2} \left[ \sqrt{(2\hbar v_\tau k + \beta\gamma\lambda_\sigma)^2 + \lambda_\tau^2} + \gamma \sqrt{(2\hbar v_\sigma k + \beta\gamma\lambda_\tau)^2 + \lambda_\sigma^2} \right], \quad (19a)$$

$$E_{\alpha,\beta}^O(\mathbf{k}) = \alpha \left[ (\hbar v_\sigma k)^2 + (3t_0 \Delta)^2 + \frac{\lambda_\tau^2}{8} + \beta\lambda_\sigma \sqrt{(\hbar v_\sigma k)^2 + \left(\frac{\lambda_\sigma}{2}\right)^2} \right]^{1/2}, \quad (19b)$$

where the indices  $\alpha, \beta, \gamma = \pm 1$ . Note that in the Kek-Y case, the dispersions are identical for  $n = \pm 1$ . Figure 1 shows the band structure (19a) along the  $\overline{-M\Gamma M}$  line ( $k_y = 0$ ) of the KBZ for different values of the RSO coupling  $\lambda_\sigma$  and Kekulé hopping modulation  $\Delta$ , keeping the Rashba modulation parameter  $\xi = 0$ . Setting  $\Delta = 0$  for finite  $\lambda_\sigma$ , we obtain the well-known band structure of RSO-coupled graphene [22,34], except folded onto the KBZ, leading to a double degeneracy for each band, corresponding to the valley pseudospin. Figure 1(a) also shows the expectation values of the  $\mathbf{s}$  and  $\boldsymbol{\sigma}$  operators as blue circled symbols and red arrows, respectively, showing that the sublattice polarization for all bands is locked perpendicularly to the spin, forming a right-handed (left-handed) pair [35] for the first conduction and second valence (second conduction and first valence) bands, with the sublattice (spin) vector always pointing in the radial (polar) direction.

Figure 1(b) shows the case of  $\lambda_\sigma = 0$  with a finite Kekulé hopping modulation  $\Delta$ , reproducing the band structure of ordinary Kek-Y graphene [21], consisting of two concentric Dirac cones with different Fermi velocities,  $v_\sigma \pm v_\tau$ . All bands are spin degenerate and valley sublattice locked into parallel (second conduction and valence bands) or antiparallel (first conduction and valence bands) pairs, with both vectors always oriented radially. This is shown in Fig. 1(b), where the

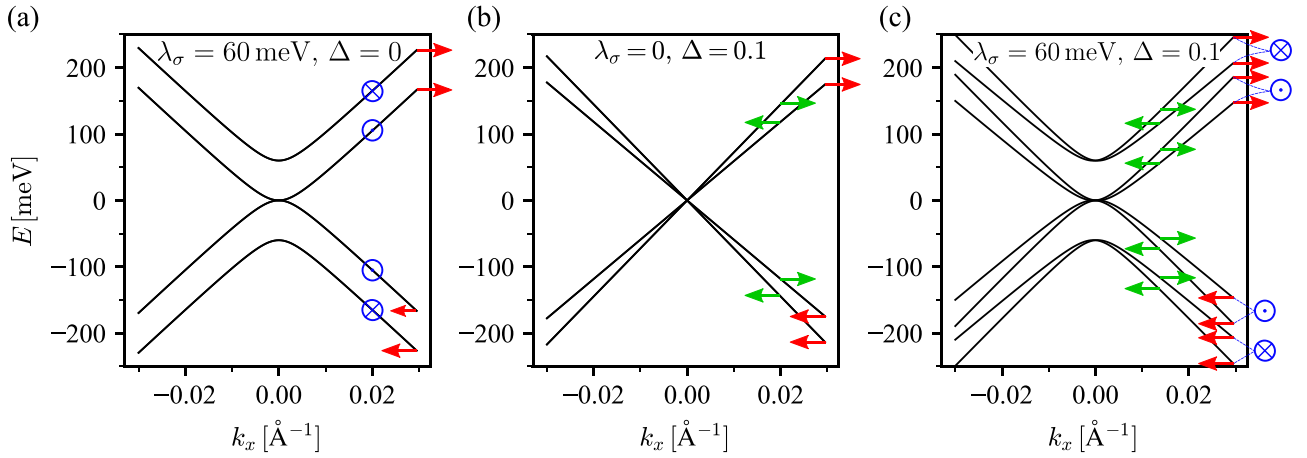


FIG. 1. Band structure (19a) for Kek-Y graphene for the parameters (a)  $\lambda_\sigma \neq 0$  and  $\Delta = 0$ , (b)  $\lambda_\sigma = 0$  and  $\Delta \neq 0$ , and (c)  $\lambda_\sigma \neq 0$  and  $\Delta \neq 0$ . In all cases, the Kekulé-induced modulation to the RSO coupling was set to  $\xi = 0$ . Blue circled symbols and red and green arrows indicate the spin, sublattice, and valley polarizations, respectively, with  $\otimes$  and  $\ominus$  representing arrows pointing in the positive and negative  $\hat{y}$  directions, respectively.

sublattice and valley vectors are shown with red and green arrows, respectively.

Next, Fig. 1(c) shows the band structure for Kek-Y graphene ( $\Delta \neq 0$ ) with finite RSO coupling ( $\lambda_\sigma \neq 0$ ). In this case, all bands show both valley-sublattice locking, as in the case of ordinary Kek-Y graphene, and spin-sublattice locking coming from the RSO interaction. The combined effect of the Kek-Y and RSO terms is thus an indirect spin-valley locking for each low-energy band at every KBZ momentum, such that once its spin polarization is known, it unequivocally determines its valley polarization. Specifically, the spin and valley vectors form right-handed pairs for the second and third conduction and first and fourth valence bands and left-handed pairs for all other bands. We point out that this spin-valley locking effect occurs even when the prefactor  $\lambda_\tau$  of the explicit spin-valley coupling in Eq. (17) vanishes.

Figure 2 shows how a finite spin-valley coupling  $\lambda_\tau = \xi \lambda_\sigma$ , coming from the Kekulé-induced modulation to the RSO interaction, modifies the band structure of Kek-Y graphene, focusing on the first two conduction and valence bands and choosing large values  $|\xi| = 0.2, 0.4$  to clearly see its effects on the band structure. For either positive or negative  $\xi$ , Fig. 2 reveals the appearance of a doubly degenerate Dirac cone centered at the  $\Gamma$  point, surrounded by a circular band touching at the Fermi level centered also at  $\Gamma$ , with bands that disperse linearly in the radial direction away from the touching points. The resulting Fermi surface is a doubly degenerate circle surrounding a fourfold-degenerate point at  $\Gamma$ . The radius of the Fermi circle increases with  $|\xi|$ , and the case  $\xi = 0$  represents a critical point where the Fermi surface becomes an eightfold-degenerate point at  $\Gamma$ . We note that all band structures in Figs. 1 and 2 are particle-hole symmetric as a consequence of the chiral symmetry  $\{\mathcal{H}_Y(\mathbf{k}), \tau_z \sigma_z s_0\} = 0$ , which we have found to hold for the Hamiltonian (17). This chirality operator was first identified by Gamayun *et al.* [21] for ordinary Kek-Y graphene ( $\lambda_\sigma = 0$ ).

For completeness, Fig. 3 shows the band structures of Kek-O graphene for  $\lambda_\sigma = 0$  and 120 meV and fixed  $\Delta = 0.1$ . It exhibits a large, direct band gap of size  $6t_0\Delta \approx 1.9$  eV at the  $\Gamma$

point, coming from the valley-sublattice coupling in Eq. (18). For  $\lambda_\sigma = 0$ , the conduction and valence bands are parabolic, whereas for finite  $\lambda_\sigma$  we obtain the typical band structure of RSO-coupled parabolic bands. Note that the Kekulé-induced Rashba modulation  $\xi$  does not appear in the Kek-O Hamiltonian (18). Henceforth, we shall focus on the Kek-Y case, which we deem more interesting due to its lack of a band gap and the chiral nature of its bands.

### III. LANDAU LEVEL SPECTRUM OF KEK-Y GRAPHENE WITH RSO COUPLING

We introduce an out-of-plane magnetic field  $\mathbf{B} = B\hat{z}$ , with symmetric-gauge vector potential  $\mathbf{A} = \frac{B}{2}(-y\hat{x} + x\hat{y})$ , into the Kek-Y graphene Hamiltonian (17) [36] via the minimal substitution  $\hbar\mathbf{k} \rightarrow \hbar\mathbf{k} - \frac{e}{c}\mathbf{A} = \boldsymbol{\pi}$ , where the components of the canonical momentum  $\boldsymbol{\pi}$  obey the algebra  $[\pi_x, \pi_y] = -i\frac{e}{c}\hbar B$ . This allows the introduction of the ladder operators ( $\pi_\pm \equiv \pi_x \pm i\pi_y$ )

$$a = \sqrt{\frac{c}{2e\hbar B}}\pi_-, \quad a^\dagger = \sqrt{\frac{c}{2e\hbar B}}\pi_+, \quad (20)$$

obeying the harmonic oscillator algebra  $[a, a^\dagger] = 1$  and operating on the LL basis  $\{|l\rangle\}$  as  $a|l\rangle = \sqrt{l}|l-1\rangle$  and  $a^\dagger|l\rangle = \sqrt{l+1}|l+1\rangle$  for integer  $l \geq 0$ . These operators enter the Kek-Y Hamiltonian (17) through the substitution

$$\boldsymbol{\pi} \cdot \mathbf{v} = \pi_+ v_- + \pi_- v_+ = \sqrt{\frac{2e\hbar B}{c}}(a^\dagger v_- + a v_+), \quad (21)$$

where  $\mathbf{v} = \boldsymbol{\tau}, \boldsymbol{\sigma}$ . The resulting LL Hamiltonian is shown in its full form in Appendix B. Here, we merely report its numerical energy spectra for varying magnetic field.

Figure 4(a) shows the LLs obtained in the absence of a Kek-Y deformation for multiple values of the RSO coupling  $\lambda_\sigma$ , including  $\lambda_\sigma = 0$ , which corresponds to the case of pristine graphene. In that case [37], a fourfold-degenerate zero-energy mode appears for all magnetic field values, surrounded by an electron-hole-symmetric fan of valley- and spin-degenerate LLs evolving as  $B^{1/2}$ . The zero modes persist

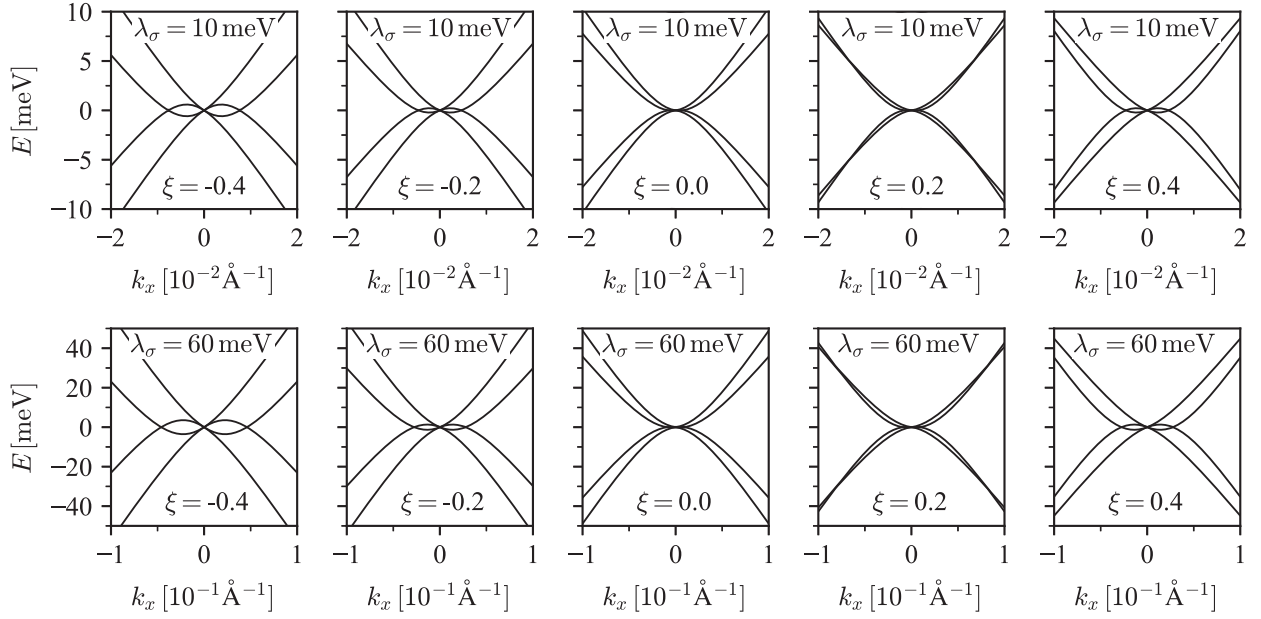


FIG. 2. Low-energy bands of Kek-Y graphene for different values of the Kekulé-induced RSO modulation  $\xi$  for fixed  $\Delta = 0.1$  and  $\lambda_\sigma = 10$  meV (top row) and  $\lambda_\sigma = 60$  meV (bottom row). Note the qualitative similarities between the two cases when both axes are appropriately rescaled.

for finite  $\lambda_\sigma$ , and the surrounding LLs split into two distinct fans, corresponding to the two separate conduction and valence bands shown in Fig. 1(a). As a connection with transport experiments, Fig. 4(b) shows the density of states (DOS) at the Fermi level as a function of both magnetic field and  $\lambda_\sigma$ , with  $\varepsilon_F = 50$  meV.

Next, Fig. 5 shows the LL spectrum of Kek-Y graphene for multiple values of  $\Delta$ , with  $\lambda_\sigma = \xi = 0$ , showing that the zero-mode quadruplet also survives in the presence of the Kekulé deformation, as reported in Ref. [21]. The reference LL fan of pristine graphene splits into two separate fans when  $\Delta \neq 0$ . Note, however, that this splitting occurs only at finite

magnetic fields, and both fans evolve with magnetic field as  $B^{1/2}$ , by contrast to the case of Rashba-SO-coupled graphene. This is a consequence of the two Dirac cones with different Fermi velocities  $v_\sigma \pm v_\tau$ , shown in Fig. 1(b). Figure 5(b) shows the Fermi level DOS for  $\varepsilon_F = 50$  meV, as it evolves with the Kekulé hopping modulation  $\Delta$ . Importantly, we can see that the DOS peaks split with increasing  $\Delta$ , analogous to the case of RSO coupling shown in Fig. 4(b). In other words, a splitting in the DOS peaks, measured in magnetotransport experiments as split conductance peaks, may come from either source. However, as we discuss next, the two effects can be distinguished through doping-dependent transport measurements. For completeness, the LL spectrum of graphene with both a Kek-Y distortion and RSO coupling is shown in Appendix C. Figure 6 shows the DOS at the Fermi level for varying magnetic field  $B$  and Fermi energy  $\varepsilon_F$  while the model parameters in (17) are kept constant, with  $\xi = 0$  in all cases. Qualitatively similar behaviors are observed both for finite  $\lambda_\sigma$  and no Kek-Y distortion (left panels) and for no RSO coupling with finite Kek-Y distortion (right panels), namely, a fan of LLs that split into two, with overall larger splittings obtained for larger values of the finite parameter. Some of these splittings are indicated in Fig. 6(h). However, we have found that the  $\varepsilon_F$  dependence of these splittings is distinct for the cases of ( $\lambda_\sigma \neq 0$ ,  $\Delta = 0$ ) and ( $\lambda_\sigma = 0$ ,  $\Delta \neq 0$ ).

Figure 7 shows the LL magnetic field splittings of the bottom three split pairs indicated in Fig. 6(h) as a function of the Fermi energy. Figure 7(a) shows that, for a pure Kek-Y distortion ( $\lambda_\sigma = 0$ ), all three splittings exhibit a power-law behavior

$$\delta B_\rho(\varepsilon_F) = A_\rho \varepsilon_F^2, \quad (22)$$

where  $\rho = \blacksquare, \blacktriangle, \blacklozenge$  indicates the corresponding magnetic field splitting shown in Fig. 6. For instance, for the rightmost splitting one can analytically compute the coefficient (see

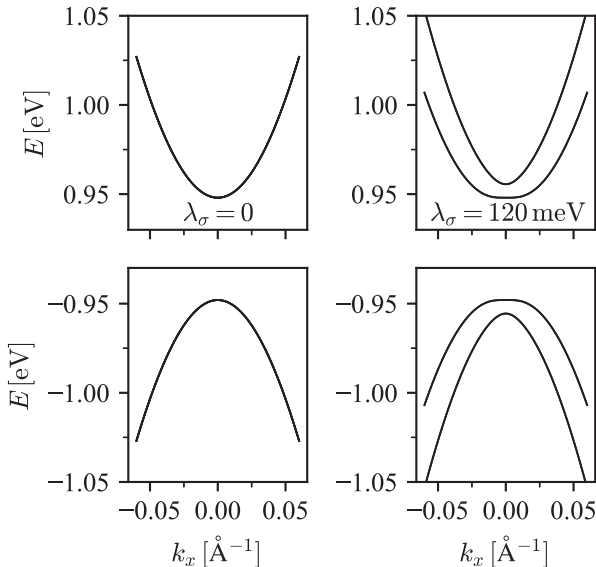


FIG. 3. Band structures of the Hamiltonian (18) for Kek-O graphene for RSO coupling  $\lambda_\sigma = 0$  and 120 meV for fixed  $\Delta = 0.1$ .

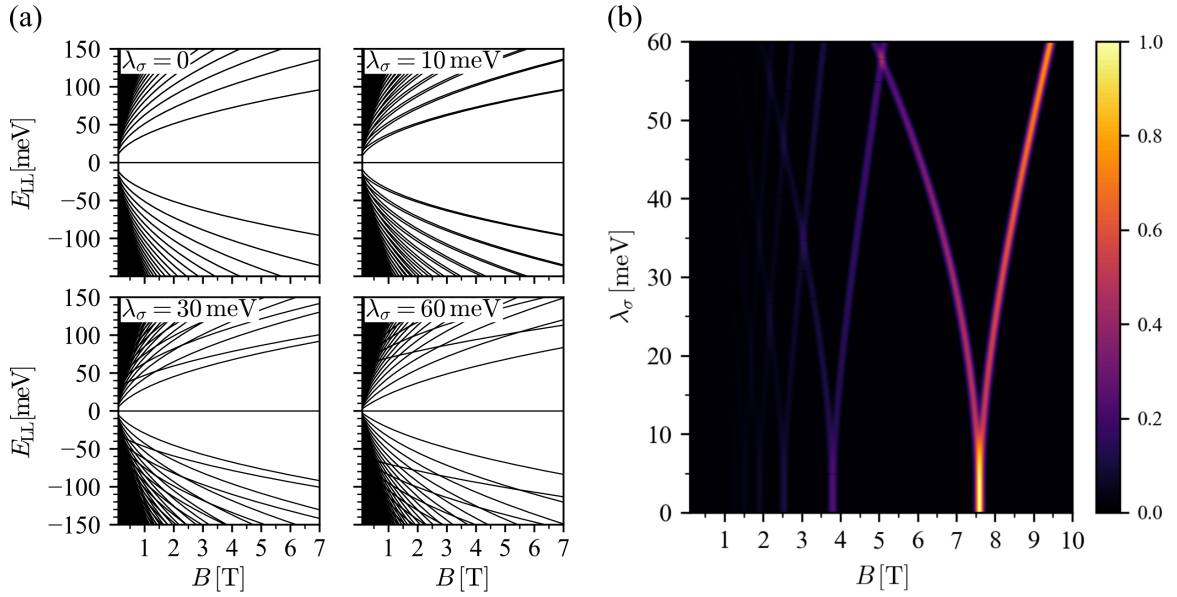


FIG. 4. (a) Landau levels for different values of  $\lambda_\sigma$  and (b)  $B^2 \times \text{DOS}(\epsilon_F)$  (arbitrary units) as a function of  $\lambda_\sigma$  and magnetic field for  $\Delta = \xi = 0$ . In (b) we set  $\epsilon_F = 50$  meV.

#### Appendix D

$$A_{\blacksquare} = \frac{8\Delta^2}{\hbar^2 v_F^2} \sqrt{\frac{c}{2e\hbar}} \quad (23)$$

up to third order in  $\Delta$ . By contrast, Fig. 7(b) shows that, in the case of pure RSO coupling ( $\Delta = 0$ ), there is clear saturation of the splitting energies at large  $\epsilon_F$ , with the first LL splitting (symbol  $\blacksquare$ ) showing saturation already for  $\epsilon_F \approx 50$  meV. The saturation value of the first LL splitting can be computed as (see Appendix D)

$$\delta B_{\blacksquare}(\epsilon_F \gg \lambda_\sigma) = \frac{2\lambda_\sigma^2}{\hbar^2 v_\sigma^2} \sqrt{\frac{c}{2e\hbar}}. \quad (24)$$

We propose that these distinct behaviors may be used experimentally not only to distinguish between the two effects but also to estimate the magnitude of the Kekulé distortion or RSO coupling using doping-dependent magnetotransport measurements.

Figure 7(c) shows the predicted magnetic field splittings for a graphene sample with both a Kek-Y distortion and finite RSO coupling, the latter without Kekulé modulation ( $\xi = 0$ ). Although the analysis that led us to Eqs. (23) and (24) can be repeated in this case, the resulting expressions are much more complicated and far less illuminating. Nonetheless, the simultaneous presence of both the Kek-Y distortion and the Rashba effect can be inferred from the first ( $\blacksquare$ ) splitting:

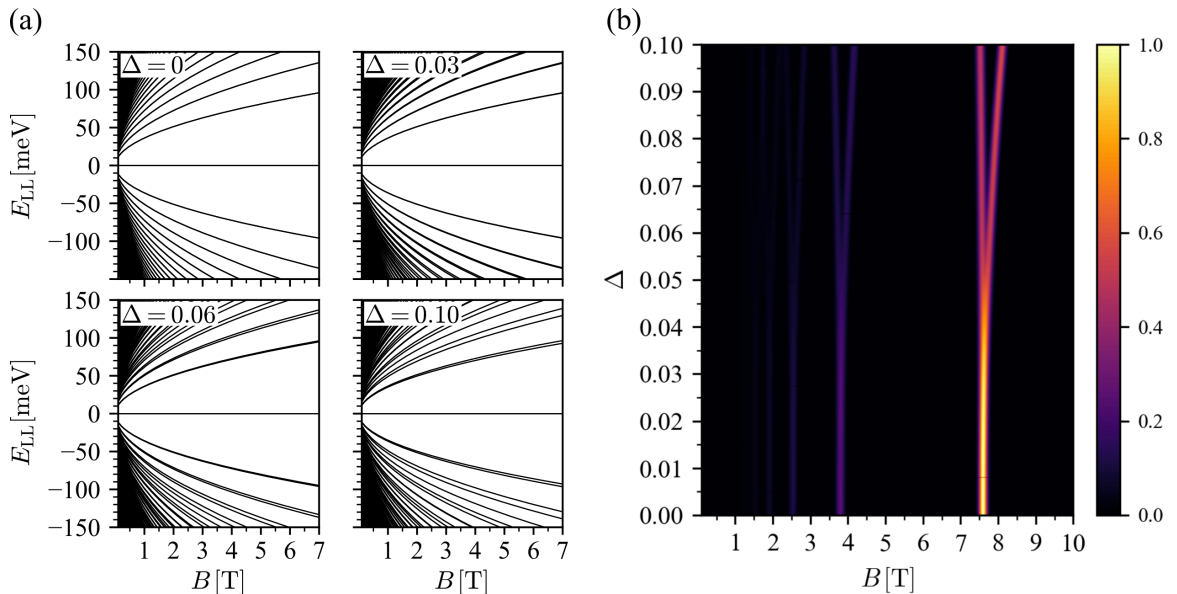


FIG. 5. (a) Landau levels for different values of  $\Delta$  and (b)  $B^2 \times \text{DOS}(\epsilon_F)$  (arbitrary units) as a function of  $\Delta$  and magnetic field for  $\lambda_\sigma = \xi = 0$ . In (b) we set  $\epsilon_F = 50$  meV.

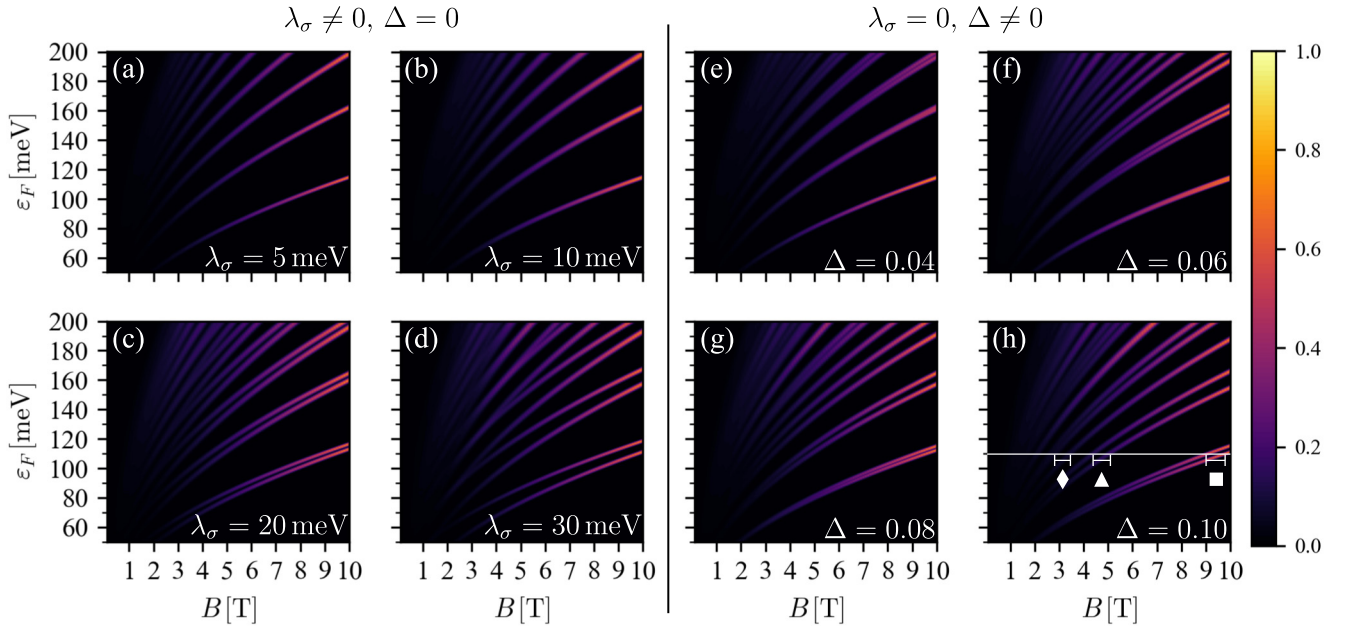


FIG. 6.  $B^2 \times \text{DOS}(\varepsilon_F)$  as a function of the Fermi energy  $\varepsilon_F$  and magnetic field  $B$  for  $\xi = 0$ . Left (right) panels correspond to model (17) with  $\Delta = 0$  ( $\Delta \neq 0$ ). The markers in (h) indicate the splittings described in Fig. 7.

Fig. 7(c) shows a crossover from a saturating behavior at low  $\varepsilon_F$ , consistent with  $\lambda_\sigma \neq 0$ , to a monotonic increase at large  $\varepsilon_F$  when the Kek-Y distortion begins to dominate. Importantly, note that the initial plateau that appears before the crossover exceeds the theoretical value for the case of only RSO coupling (24), shown by the cyan line in Fig. 7(c). Therefore, when aiming to determine the values of the Hamiltonian parameters  $\lambda_\sigma$  and  $\Delta$  from magnetotransport experiments, it is important to explore beyond the weak doping regime to avoid overestimating the value of  $\lambda_\sigma$ .

Finally, we briefly discuss the case where all Kek-Y model parameters  $\lambda_\sigma$ ,  $\Delta$ , and  $\xi$  are finite. The corresponding LL spectrum is shown in Fig. 8 in Appendix C. In this case, the LL structure is quite complex, and a doping-dependent magnetic field splitting analysis becomes intractable. However, the new dispersion has a salient feature that is absent when either  $\Delta = 0$  or  $\lambda_\sigma = 0$ , namely, that the zero-energy quadruplet shown in Figs. 4(a) and 5(a) splits for finite magnetic fields into a zero-energy doublet, closely surrounded by two electron-hole-symmetric LLs. For small values of  $|\Delta - \xi|$ , the

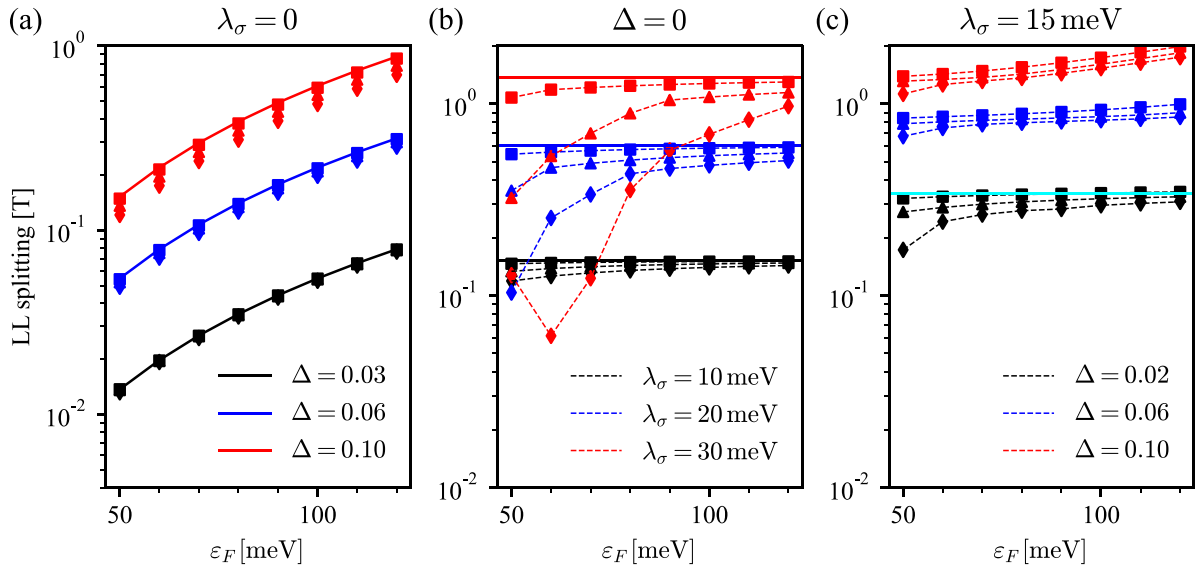


FIG. 7. Energy splittings of the lower three LL pairs as a function of the Fermi energy  $\varepsilon_F$  for fixed model parameters (a) ( $\lambda_\sigma = 0$ ,  $\Delta \neq 0$ ), (b) ( $\lambda_\sigma \neq 0$ ,  $\Delta = 0$ ), and (c) ( $\lambda_\sigma \neq 0$ ,  $\Delta \neq 0$ ), with  $\xi = 0$  in all cases. The data symbols ( $\blacksquare$ ,  $\blacktriangle$ , and  $\blacklozenge$ ) are matched to those shown in Fig. 6(h). The solid lines in (a) correspond to Eq. (22) with the coefficient  $A_{\blacksquare}$  given by Eq. (23), whereas in (b) the solid lines indicate the saturation value given by Eq. (24). The cyan solid line in (c) indicates the saturation value predicted by Eq. (24), which is exceeded in the presence of a Kek-Y distortion. The dashed lines in (b) and (c) are merely guides to the eye.

splitting between the latter two LLs takes the form  $[v_\sigma(B) \equiv v_\sigma \sqrt{\frac{2e\hbar B}{c}}]$ ; see Appendix B]

$$\delta\varepsilon_{z'} = \frac{2\lambda_\sigma v_\sigma(B)}{\sqrt{(1+\Delta^2)v_\sigma^2(B) + (1+\xi^2)\lambda_\sigma^2}} |\Delta - \xi| \quad (25)$$

and is always finite, with the exception of the fine-tuned case  $\Delta = \xi$ . It is possible that this feature may be observed in magnetotransport experiments at very low doping levels, thus confirming that both a Kekulé-Y texture and finite RSO coupling are present in the graphene system. Moreover, if the parameters  $\Delta$  and  $\lambda_\sigma$  are estimated from the previously discussed analysis of the magnetic field splittings, they may be introduced into Eq. (25), thus allowing for a rough estimation of the RSO modulation parameter  $\xi$ .

#### IV. CONCLUSIONS

We introduced generalized tight-binding Hamiltonians for graphene with Kekulé-Y and Kekulé-O bond textures, as well as Rashba spin-orbit coupling, which takes into account a possible modulation of the Rashba term by the Kekulé bond distortions. We also derived low-energy effective models based on the general tight-binding Hamiltonians, following the scheme introduced by Gamayun *et al.* [21]. We found that, whereas the Kekulé-O effective model is independent of the Rashba term modulation, the Kekulé-Y model exhibits novel spin-valley locking, as well as a new combined Kekulé-Rashba term that can dramatically modify the Fermi surface of the system in charge neutrality.

We also studied the Landau level spectrum of this system under a perpendicular magnetic field and computed its density of states at the Fermi level with an aim to motivate magnetotransport experiments on Kekulé graphene systems on transition metal substrates. We found that, whereas the Landau level spectra exhibit a degenerate quadruplet of zero-

energy modes in graphene with either a Kekulé-Y distortion or Rashba spin-orbit coupling, this degeneracy is partially lifted when both effects are present, resulting in a degenerate doublet of zero-energy modes closely surrounded by two satellite Landau levels. Based on our findings, we put forth an experimental method to distinguish the presence of the Kekulé-Y bond texture, a Rashba spin-orbit term, or both based on an analysis of the magnetic field splittings of the DOS peaks as a function of the Fermi energy. We showed that, once the strengths of both effects are extracted from this analysis, they may be used to estimate the magnitude of the Kekulé-induced modulation of the Rashba spin-orbit coupling based on the magnitude of the zero-energy mode splitting, which may be experimentally resolved at low enough values of the Fermi energy.

Possible realizations of the models presented in this paper are sandwich-type Cu-graphene- $M$ , where  $M$  represents a heavy transition metal with a large spin-orbit interaction, such as gold [22] and iridium [38], and the graphene sample has been epitaxially grown on top of a copper substrate. Such systems may combine the two basic ingredients required for our model: A Kekulé distortion and a proximity-induced Rashba interaction. A possible alternative may be to deposit gold nanoparticles onto a Kekulé graphene system, such as epitaxial Cu-graphene, or even lithium intercalated graphene. It was recently shown [20] that gold nanoparticles deposited onto graphene naturally adopt a Kekulé configuration, opening a possible pathway to introducing the spatially modulated Rashba interaction considered in our models.

#### ACKNOWLEDGMENTS

D.A.R.-T. acknowledges funding from PAPIIT-DGAPA-UNAM through Project No. IA106523. F.M. acknowledges funding from PAPIIT-DGAPA-UNAM through Projects No. IN113920 and No. IN111624.

#### APPENDIX A: EFFECTIVE LOW-ENERGY BLOCH HAMILTONIANS

Starting from Eq. (12), we identify the four high-energy bands corresponding to states at the  $\Gamma$  point of the original BZ and neglect them, which corresponds to projecting them out at zeroth order in perturbation theory. This is justified by the large offset between these states and the Fermi level ( $\approx 3$  eV) compared with all relevant model parameters, which fall in the 10 meV range. Collecting the annihilation operators in the column vector  $\psi_{\mathbf{k}} = (a_{\mathbf{k}-\mathbf{G},\uparrow}, a_{\mathbf{k}-\mathbf{G},\downarrow}, a_{\mathbf{k}+\mathbf{G},\uparrow}, a_{\mathbf{k}+\mathbf{G},\downarrow}, b_{\mathbf{k}-\mathbf{G},\uparrow}, b_{\mathbf{k}-\mathbf{G},\downarrow}, b_{\mathbf{k}+\mathbf{G},\uparrow}, b_{\mathbf{k}+\mathbf{G},\downarrow})^T$ , we write the total Hamiltonian for the eight bands closest to the Fermi level as

$$\mathcal{H}'_{pq}(\mathbf{k}) = \begin{pmatrix} 0 & \Sigma_n(\mathbf{k}) \\ \Sigma_n^\dagger(\mathbf{k}) & 0 \end{pmatrix}, \quad (A1)$$

with  $n$  given by the Kekulé texture parameters  $p$  and  $q$  through Eq. (5) and

$$\Sigma_n(\mathbf{k}) = \begin{pmatrix} \Phi_{-1}(\mathbf{k}) & i\Lambda_{-1}^{\uparrow\downarrow}(\mathbf{k}) & \Delta\Phi_n(\mathbf{k}) & i\xi\Lambda_n^{\uparrow\downarrow}(\mathbf{k}) \\ i\Lambda_{-1}^{\downarrow\uparrow}(\mathbf{k}) & \Phi_{-1}(\mathbf{k}) & i\xi\Lambda_n^{\downarrow\uparrow}(\mathbf{k}) & \Delta\Phi_n(\mathbf{k}) \\ \Delta^*\Phi_{-n}(\mathbf{k}) & i\xi^*\Lambda_{-n}^{\uparrow\downarrow}(\mathbf{k}) & \Phi_1(\mathbf{k}) & i\Lambda_1^{\uparrow\downarrow}(\mathbf{k}) \\ i\xi^*\Lambda_{-n}^{\downarrow\uparrow}(\mathbf{k}) & \Delta^*\Phi_n(\mathbf{k}) & i\Lambda_1^{\downarrow\uparrow}(\mathbf{k}) & \Phi_1(\mathbf{k}) \end{pmatrix}, \quad (A2)$$



where  $\Phi_n(\mathbf{k}) = \Phi_n(\mathbf{k} + n\mathbf{G})$  and  $\Lambda_n^{\mu\nu}(\mathbf{k}) = \Lambda_{\mu\nu}(\mathbf{k} + n\mathbf{G})$ , following the definitions (9). For  $\mu \neq \nu$  we obtain explicitly

$$\Lambda_0^{\mu\nu}(\mathbf{k}) = \frac{\lambda_\sigma}{3} e^{ia_0k_y} \left[ 1 + 2 \cos \left( \frac{\sqrt{3}}{2} a_0 k_x + \frac{2\pi}{3} \gamma_{\mu\nu} \right) e^{-i\frac{3}{2} a_0 k_y} \right], \quad (\text{A3a})$$

$$\Lambda_{\pm 1}^{\mu\nu}(\mathbf{k}) = \frac{\lambda_\sigma}{6} e^{-ia_0k_y} \left[ (1 \mp 3) \cos \left( \frac{\sqrt{3}}{2} a_0 k_x \right) + \sqrt{3} (\gamma_{\mu\nu} \pm 1) \sin \left( \frac{\sqrt{3}}{2} a_0 k_x \right) + 2e^{ia_0k_y} \right], \quad (\text{A3b})$$

where we have defined  $\gamma_{\uparrow\downarrow} = -\gamma_{\downarrow\uparrow} = 1$ . Moreover,  $\Lambda_n^{\mu\mu}(\mathbf{k}) = 0$ .

We now focus on momenta close to the KBZ  $\Gamma$  point and expand all expressions up to first order in  $a_0\mathbf{k}$  to obtain ( $\hbar v_\sigma = \frac{3}{2} a_0 t_0$ )

$$\Phi_0(\mathbf{k}) \approx -3t_0, \quad (\text{A4a})$$

$$\Phi_{\pm 1}(\mathbf{k}) \approx \hbar v_\sigma (\mp k_x + ik_y), \quad (\text{A4b})$$

$$\Lambda_0^{\uparrow\downarrow}(\mathbf{k}) = -(\Lambda_0^{\downarrow\uparrow}(\mathbf{k}))^* \approx -\frac{\lambda_\sigma}{2} a_0 (k_x - ik_y), \quad (\text{A4c})$$

$$\Lambda_1^{\uparrow\downarrow}(\mathbf{k}) = -(\Lambda_{-1}^{\downarrow\uparrow}(\mathbf{k}))^* \approx \frac{\lambda_\sigma}{2} a_0 (k_x + ik_y), \quad (\text{A4d})$$

$$\Lambda_{-1}^{\uparrow\downarrow}(\mathbf{k}) = \Lambda_1^{\downarrow\uparrow}(\mathbf{k}) \approx \lambda_\sigma. \quad (\text{A4e})$$

For clarity, we now use the basis ordering chosen in Ref. [21] for each spin quantum number,  $\psi'_{\mathbf{k}} = (\psi'_{\mathbf{k},\uparrow}, \psi'_{\mathbf{k},\downarrow})^T$ , with ( $s = \uparrow, \downarrow$ )

$$\psi_{\mathbf{k},s} = (-b_{\mathbf{k}-\mathbf{G},s}, a_{\mathbf{k}-\mathbf{G},s}, a_{\mathbf{k}+\mathbf{G},s}, b_{\mathbf{k}+\mathbf{G},s})^T,$$

such that the effective Hamiltonian adopts the form

$$\mathcal{H}_{pq}''(\mathbf{k}) = \begin{pmatrix} \mathcal{H}_0^{pq}(\mathbf{k}) & 0_{4 \times 4} \\ 0_{4 \times 4} & \mathcal{H}_0^{pq}(\mathbf{k}) \end{pmatrix} + \begin{pmatrix} 0_{4 \times 4} & \mathcal{H}_R^{pq}(\mathbf{k}) \\ \mathcal{H}_R^{pq\dagger}(\mathbf{k}) & 0_{4 \times 4} \end{pmatrix}, \quad (\text{A5})$$

where

$$\mathcal{H}_0^{pq}(\mathbf{k}) = \begin{pmatrix} \hbar v_\sigma \mathbf{k} \cdot \boldsymbol{\sigma} & \Delta Q_n(\mathbf{k}) \\ \Delta^* Q_n^\dagger(\mathbf{k}) & \hbar v_\sigma \mathbf{k} \cdot \boldsymbol{\sigma} \end{pmatrix} \quad (\text{A6})$$

is the usual Kekulé graphene Hamiltonian for either a Kek-O ( $Q_0 = 3t_0\sigma_z$ ) or a Kek-Y [ $Q_{\pm 1} = \hbar v_\sigma (\pm k_x - ik_y)\sigma_0$ ] texture. The Kekulé-RSO term  $\mathcal{H}_R^{pq}(\mathbf{k})$  has the general form

$$\mathcal{H}_R^{pq}(\mathbf{k}) = \begin{pmatrix} 0 & i[\Delta_{-1}^{\downarrow\uparrow}(\mathbf{k})]^* & i\xi[\Delta_{-n}^{\downarrow\uparrow}(\mathbf{k})]^* & 0 \\ -i\Delta_{-1}^{\uparrow\downarrow}(\mathbf{k}) & 0 & 0 & i\xi\Delta_n^{\uparrow\downarrow}(\mathbf{k}) \\ -i\xi^*\Delta_{-n}^{\uparrow\downarrow}(\mathbf{k}) & 0 & 0 & i\Delta_1^{\uparrow\downarrow}(\mathbf{k}) \\ 0 & -i\xi^*[\Delta_n^{\downarrow\uparrow}(\mathbf{k})]^* & -i[\Delta_1^{\downarrow\uparrow}(\mathbf{k})]^* & 0 \end{pmatrix}$$

and simplifies as follows for the three possible values  $n = -1, 0, 1$ : For  $n = 0$  we get the Kek-O effective model

$$\mathcal{H}_R^{n=0}(\mathbf{k}) = \begin{pmatrix} 0 & -i\frac{\lambda_\sigma}{2} a_0 (k_x + ik_y) & i\xi\frac{\lambda_\sigma}{2} a_0 (k_x - ik_y) & 0 \\ -i\lambda_\sigma & 0 & 0 & -i\xi\frac{\lambda_\sigma}{2} a_0 (k_x - ik_y) \\ i\xi^*\frac{\lambda_\sigma}{2} a_0 (k_x - ik_y) & 0 & 0 & i\frac{\lambda_\sigma}{2} a_0 (k_x + ik_y) \\ 0 & -i\xi^*\frac{\lambda_\sigma}{2} a_0 (k_x - ik_y) & -i\lambda_\sigma & 0 \end{pmatrix}, \quad (\text{A7})$$

whereas for  $n = \pm 1$  we obtain the Kek-Y effective models

$$\mathcal{H}_R^{n=\pm 1}(\mathbf{k}) = \begin{pmatrix} 0 & -i\frac{\lambda_\sigma}{2} a_0 (k_x + ik_y) & -i\xi\frac{\lambda_\sigma}{2} a_0 (k_x + ik_y) & 0 \\ -i\lambda_\sigma & 0 & 0 & i\xi\frac{\lambda_\sigma}{2} a_0 (k_x + ik_y) \\ -i\xi^*\lambda_\sigma & 0 & 0 & i\frac{\lambda_\sigma}{2} a_0 (k_x + ik_y) \\ 0 & -i\xi^*\lambda_\sigma & -i\lambda_\sigma & 0 \end{pmatrix}, \quad (\text{A8a})$$

$$\mathcal{H}_R^{n=-1}(\mathbf{k}) = \begin{pmatrix} 0 & -i\frac{\lambda_\sigma}{2}a_0(k_x + ik_y) & i\xi\lambda_\sigma & 0 \\ -i\lambda_\sigma & 0 & 0 & i\xi\lambda_\sigma \\ -i\xi^*\frac{\lambda_\sigma}{2}a_0(k_x + ik_y) & 0 & 0 & i\frac{\lambda_\sigma}{2}a_0(k_x + ik_y) \\ 0 & i\xi^*\frac{\lambda_\sigma}{2}a_0(k_x + ik_y) & -i\lambda_\sigma & 0 \end{pmatrix}. \quad (\text{A8b})$$

Equations (17) and (18) are obtained from Eqs. (A8) and (A7), respectively, by reordering the basis according to Eq. (16) and neglecting the terms linear in momentum.

### APPENDIX B: LANDAU LEVEL HAMILTONIAN FOR THE KEK-Y CASE

For the Kekulé-Y case, the electronic Hamiltonian is obtained from (17) by substituting [31,39]

$$\begin{aligned} \hbar v_\sigma(k_x + ik_y) &\longrightarrow v_\sigma(B)a^\dagger, \\ \hbar v_\sigma(k_x - ik_y) &\longrightarrow v_\sigma(B)a, \end{aligned}$$

with  $v_\sigma(B) \equiv v_\sigma \sqrt{\frac{2e\hbar B}{c}}$  (in Gaussian units) and  $a$  and  $a^\dagger$  being the LL ladder operators. Ordering the basis as

$$\begin{aligned} &\{|\uparrow, 1, -1\rangle, |\uparrow, -1, 1\rangle, |\downarrow, 1, -1\rangle, |\downarrow, -1, 1\rangle, \\ &|\uparrow, -1, -1\rangle, |\uparrow, 1, 1\rangle, |\downarrow, -1, -1\rangle, |\downarrow, 1, 1\rangle\}, \end{aligned}$$

where the quantum numbers correspond to spin  $s$ , pseudospin  $\sigma$ , and valley  $\tau$ , respectively, the Landau level Hamiltonian takes the form

$$H_{\text{KY}}^{\text{LL}} = \begin{pmatrix} 0 & h(B) \\ h^\dagger(B) & 0 \end{pmatrix}, \quad (\text{B1})$$

with

$$h(B) = \begin{pmatrix} v_\sigma(B)a & \Delta v_\sigma(B)a^\dagger & 0 & -i\xi\lambda_\sigma \\ \Delta v_\sigma(B)a & v_\sigma(B)a^\dagger & 0 & -i\lambda_\sigma \\ i\lambda_\sigma & 0 & v_\sigma(B)a & \Delta v_\sigma(B)a^\dagger \\ i\xi\lambda_\sigma & 0 & \Delta v_\sigma(B)a & v_\sigma(B)a^\dagger \end{pmatrix}. \quad (\text{B2})$$

Defining the Landau level eigenstates  $|s, \sigma, \tau; \ell\rangle$  ( $\ell = 0, 1, 2, \dots$ ), we may propose a general solution of the form

$$|\psi_\ell\rangle = \begin{pmatrix} |\ell - 2\rangle \\ |\ell - 2\rangle \\ |\ell - 1\rangle \\ |\ell - 1\rangle \\ |\ell - 1\rangle \\ |\ell - 1\rangle \\ |\ell - 3\rangle \\ |\ell\rangle \\ |\ell - 2\rangle \end{pmatrix}, \quad (\text{B3})$$

such that for  $\ell \geq 3$  we get

$$H_{\text{KY}}^{\text{LL}}|\psi_\ell\rangle = \begin{pmatrix} 0_{4 \times 4} & h_n(B) \\ h_n^\dagger(B) & 0_{4 \times 4} \end{pmatrix}|\psi_\ell\rangle, \quad (\text{B4})$$

with

$$h_\ell(B) = \begin{pmatrix} v_\sigma(B)\sqrt{\ell-1} & \Delta v_\sigma(B)\sqrt{\ell-2} & 0 & -i\xi\lambda_\sigma \\ \Delta v_\sigma(B)\sqrt{\ell-1} & v_\sigma(B)\sqrt{\ell-2} & 0 & -i\lambda_\sigma \\ i\lambda_\sigma & 0 & v_\sigma(B)\sqrt{\ell} & \Delta v_\sigma(B)\sqrt{\ell-1} \\ i\xi\lambda_\sigma & 0 & \Delta v_\sigma(B)\sqrt{\ell} & v_\sigma(B)\sqrt{\ell-1} \end{pmatrix}, \quad \ell \geq 3. \quad (\text{B5})$$

Setting  $\ell = 2$  yields the reduced problem

$$H_{\text{KY}}^{\text{LL}}|\psi_2\rangle = \begin{pmatrix} 0_{4 \times 4} & h_2(B) \\ h_2^\dagger(B) & 0_{3 \times 3} \end{pmatrix}|\psi_2\rangle, \quad (\text{B6})$$

with

$$h_2(B) = \begin{pmatrix} v_\sigma(B) & 0 & -i\xi\lambda_\sigma \\ \Delta v_\sigma(B) & 0 & -i\lambda_\sigma \\ i\lambda & \sqrt{2}v_\sigma(B) & \Delta v_\sigma(B) \\ i\xi\lambda_\sigma & \sqrt{2}\Delta v_\sigma(B) & v_\sigma(B) \end{pmatrix} \quad (\text{B7})$$

and the reduced basis

$$\{|\uparrow, 1, -1; 0\rangle, |\uparrow, -1, 1; 0\rangle, |\downarrow, 1, -1; 1\rangle, |\downarrow, -1, 1; 1\rangle, |\uparrow, -1, -1; 1\rangle, |\downarrow, -1, -1; 2\rangle, |\downarrow, 1, 1; 0\rangle\}. \quad (\text{B8})$$

From this case we can extract the valley-sublattice-locked ( $\tau\sigma = -1$ ) zero-energy mode

$$|z_-\rangle = N_z^{-\frac{1}{2}} [-(\Delta\alpha - \beta)|\uparrow, 1, -1; 0\rangle + (\alpha - \xi\beta)|\uparrow, -1, 1; 0\rangle + i\Delta\gamma|\downarrow, 1, -1; 1\rangle - i\gamma|\downarrow, -1, 1; 1\rangle], \quad (\text{B9})$$

where

$$\alpha = v_\sigma^2(B)(1 - \Delta^2), \quad (\text{B10a})$$

$$\beta = \lambda_\sigma^2(\xi - \Delta), \quad (\text{B10b})$$

$$\gamma = \lambda_\sigma v_\sigma(B)\Delta(1 - \xi\Delta), \quad (\text{B10c})$$

$$N_z = (\alpha^2 + \gamma^2)(1 + \Delta^2) + \beta^2(1 + \xi^2) - 2(\xi + \Delta)\alpha\beta. \quad (\text{B10d})$$

Then, setting  $\ell = 1$ , we obtain the reduced problem

$$H_{\mathcal{KY}}^{\text{LL}}|\psi_1\rangle = \begin{pmatrix} 0_{2\times 2} & h_1(B) \\ h_1^\dagger(B) & 0_{2\times 2} \end{pmatrix}|\psi_1\rangle, \quad (\text{B11})$$

with

$$h_1(B) = \begin{pmatrix} i\lambda_\sigma & v_\sigma(B) \\ i\xi\lambda_\sigma & \Delta v_\sigma(B) \end{pmatrix}, \quad (\text{B12})$$

and the reduced basis

$$\{|\downarrow, 1, -1; 0\rangle, |\downarrow, -1, 1; 0\rangle, |\uparrow, -1, -1; 0\rangle, |\downarrow, -1, -1; 1\rangle\}.$$

This can be diagonalized analytically and gives the eigenvalues ( $\eta, \zeta = \pm 1$ )

$$\varepsilon_{\eta,\zeta}(B) = \frac{\eta}{\sqrt{2}} \sqrt{(1 + \Delta^2)v_\sigma^2(B) + (1 + \xi^2)\lambda_\sigma^2 + \zeta \sqrt{[(1 + \Delta^2)v_\sigma^2(B) + (1 + \xi^2)\lambda_\sigma^2]^2 - 4\lambda_\sigma^2 v_\sigma^2(B)(\Delta - \xi)^2}}. \quad (\text{B13})$$

Two additional zero modes are recovered in the case of  $\xi = \Delta$ , corresponding to the eigenstates

$$|z'_+\rangle = \frac{v_\sigma(B)|\uparrow, -1, -1; 1\rangle - i\lambda_\sigma|\downarrow, -1, -1; 0\rangle}{\sqrt{v_\sigma^2(B) + \lambda_\sigma^2}},$$

$$|z'_-\rangle = \frac{-\Delta|\downarrow, 1, -1; 0\rangle + |\downarrow, -1, 1; 1\rangle}{\sqrt{1 + \Delta^2}},$$

which split as

$$\delta\varepsilon_{z'} = \frac{2\lambda_\sigma v_\sigma(B)}{\sqrt{(1 + \Delta^2)v_\sigma^2(B) + (1 + \xi^2)\lambda_\sigma^2}}|\Delta - \xi| \quad (\text{B14})$$

for  $0 < |\Delta - \xi| \ll 1$ .

Finally, setting  $\ell = 0$  yields the zero-energy mode

$$|z_+\rangle = |\downarrow, -1, -1; 0\rangle. \quad (\text{B15})$$

Note that in the absence of Rashba spin-orbit coupling ( $\lambda_\sigma \rightarrow 0$ ), the four zero-energy modes identified reduce to those reported by Gamayun *et al.* in Ref. [21]:

$$\begin{aligned} |z_+\rangle|_{\lambda_\sigma=0} &= |\downarrow, -1, -1; 0\rangle, \\ |z'_+\rangle|_{\lambda_\sigma=0} &= |\uparrow, -1, -1; 1\rangle, \\ |z_-\rangle|_{\lambda_\sigma=0} &= \frac{-\Delta|\uparrow, 1, -1; 0\rangle + |\uparrow, -1, 1; 0\rangle}{\sqrt{1 + \Delta^2}}, \\ |z'_-\rangle|_{\lambda_\sigma=0} &= \frac{-\Delta|\downarrow, 1, -1; 0\rangle + |\downarrow, -1, 1; 1\rangle}{\sqrt{1 + \Delta^2}}. \end{aligned}$$

### APPENDIX C: LANDAU LEVEL SPECTRUM OF KEK-Y GRAPHENE WITH RSO COUPLING

Figure 8 shows the LL spectra of Kek-Y graphene with fixed Kekulé parameter  $\Delta = 0.1$  for several values of the RSO term  $\lambda_\sigma$ , keeping the RSO distortion  $\xi = 0$ . At first sight, this LL spectrum resembles that of RSO graphene (Fig. 4), with a duplicated fan due to the two Fermi velocities introduced by the Kek-Y distortion (Fig. 5). However, a major qualitative difference from those cases is that the zero-energy quadruplet breaks, in the case of simultaneous Kek-Y and RSO effects, into a zero-energy doublet surrounded by two dispersive LLs that split according to Eq. (B14).

### APPENDIX D: MAGNETIC FIELD SPLITTINGS IN THE FERMI-LEVEL-DEPENDENT DOS OF PURE KEK-Y AND RSO SAMPLES

The high-DOS fans in Fig. 7 are direct visualizations of constant energy cuts of the LL fans in Figs. 4 and 5 for

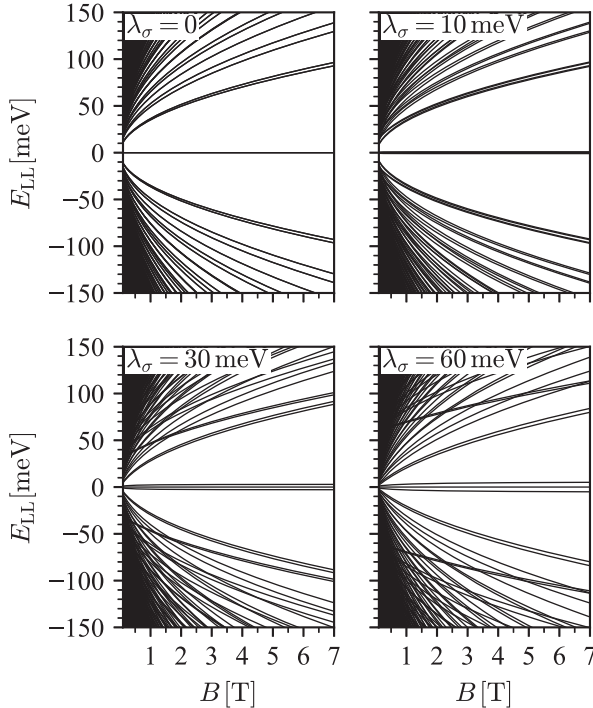


FIG. 8. Landau levels for different values of  $\lambda_\sigma$ , keeping  $\Delta = 0.1$  fixed. Note the splitting of the zero-energy quadruplet for  $\lambda_\sigma \neq 0$  into a zero-energy doublet and two dispersive LLs.

$E_{LL} = \varepsilon_F$ . The  $\varepsilon_F$ -dependent splittings can be extracted directly from the  $B$ -dependent eigenvalues of the LL Hamiltonians (B4), (B6), and (B11). For simplicity, let us focus on the rightmost LL splitting, indicated in Fig. 6(h) with the symbol ■.

In the case of only a Kek-Y distortion ( $\Delta \neq 0$ ,  $\lambda_\sigma = 0$ ,  $\xi = 0$ ), this splitting occurs between the LLs

$$\begin{aligned} \varepsilon_4^{(1)}(B) &= v_\sigma(B)\sqrt{1 + \Delta^2}, \\ \varepsilon_5^{(2)}(B) &= v_\sigma(B)\sqrt{\frac{3(1 + \Delta^2) - \sqrt{1 + 34\Delta^2 + \Delta^4}}{2}}, \end{aligned} \quad (D1)$$

where  $\varepsilon_m^{(\ell)}$  is the  $m$ th eigenvalue, with increasing energy, obtained from the model (B4) by fixing the LL index  $\ell$ . The magnetic field splitting between these two LLs at fixed  $\varepsilon_F$  is obtained as  $\delta B = B_> - B_<$ , where

$$\varepsilon_5^{(2)}(B_>) = \varepsilon_4^{(1)}(B_<) = \varepsilon_F. \quad (D2)$$

This gives

$$\begin{aligned} \delta B &= \frac{\varepsilon_F^2}{\hbar^2 v_\sigma^2} \sqrt{\frac{c}{2e\hbar}} \\ &\times \left[ \frac{2}{3(1 + \Delta^2) - \sqrt{1 + 34\Delta^2 + \Delta^4}} - \frac{1}{1 + \Delta^2} \right] \\ &= \frac{8\Delta^2}{\hbar^2 v_\sigma^2} \varepsilon_F^2 \sqrt{\frac{c}{2e\hbar}} + \mathcal{O}(\Delta^4), \end{aligned} \quad (D3)$$

leading to Eqs. (22) and (23).

We may follow the same procedure in the case of only RSO coupling ( $\Delta = 0$ ,  $\lambda_\sigma \neq 0$ ,  $\xi = 0$ ), where the relevant LL

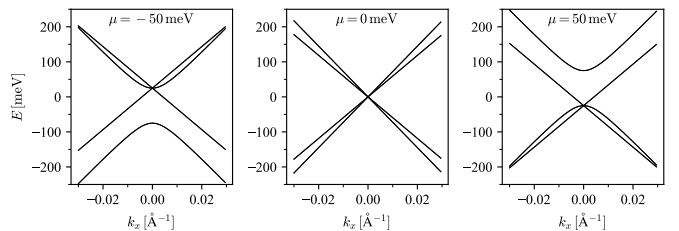


FIG. 9. Low-energy band structure for Kekulé-Y graphene with  $\Delta = 0.1$ , including the term (E1) with values of the parameter  $\mu$ .

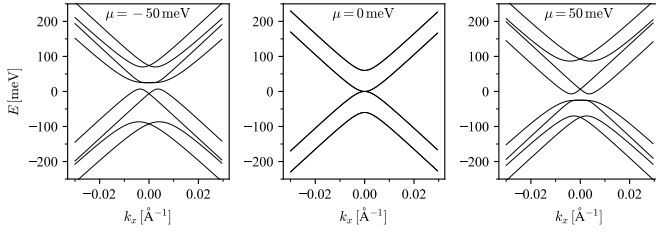


FIG. 10. Low-energy band structure for graphene with Rashba spin-orbit coupling  $\lambda_\sigma = 60$  meV, including the term (E1) with different values of the parameter  $\mu$ .

energies are

$$\begin{aligned} \varepsilon_4^{(1)}(B) &= \sqrt{\hbar^2 v_\sigma^2(B) + \lambda_\sigma^2}, \\ \varepsilon_5^{(2)}(B) &= \sqrt{\frac{3v_\sigma^2(B) + \lambda_\sigma^2 - \sqrt{v_\sigma^4(B) + 6\lambda_\sigma^2 v_\sigma^2(B) + \lambda_\sigma^4}}{2}}. \end{aligned} \quad (\text{D4})$$

In this case, Eq. (D2) gives  $B_< = \frac{\varepsilon_F^2 - \lambda_\sigma^2}{\hbar^2 v_\sigma^2} \sqrt{\frac{c}{2e\hbar}}$ , whereas for  $B_>$  we get the equation

$$\begin{aligned} 2\varepsilon_F^2 &= \lambda_\sigma^2 + (\hbar v_\sigma)^2 \sqrt{\frac{c}{2e\hbar}} B \\ &\times \left[ 3 - \sqrt{1 + \frac{6\lambda_\sigma^2}{(\hbar v_\sigma)^2 B} \sqrt{\frac{c}{2e\hbar}} + \frac{\lambda_\sigma^4}{(\hbar v_\sigma)^4 B^2} \frac{c}{2e\hbar}} \right]. \end{aligned}$$

This can be simplified by working in the limit of  $\frac{\lambda_\sigma^2}{v_\sigma^2(B)} \ll 1$  and expanding up to second order. This gives the quadratic equation

$$B^2 - \frac{\varepsilon_F^2 + \lambda_\sigma^2}{\hbar^2 v_\sigma^2} \sqrt{\frac{c}{2e\hbar}} B + \frac{2\lambda_\sigma^4}{\hbar^2 v_\sigma^4} \frac{c}{2e\hbar} \approx 0,$$

from which we take the solution

$$B_> \approx \frac{\varepsilon_F^2 + \lambda_\sigma^2}{2\hbar^2 v_\sigma^2} \left[ 1 + \sqrt{1 - \frac{8\lambda_\sigma^4}{(\varepsilon_F^2 + \lambda_\sigma^2)^2}} \right].$$

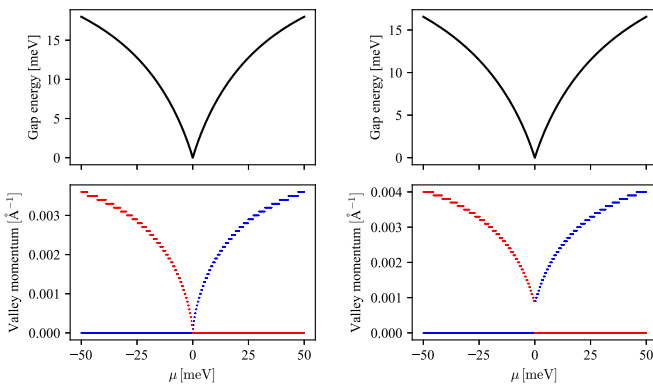


FIG. 11. Band gap and valley momentum of the conduction (blue) and valence (red) band edges as a function of  $\mu$  for the parameters  $\Delta = 0$  and  $\lambda_\sigma = 60$  meV (left) and  $\Delta = 0.1$  and  $\lambda_\sigma = 60$  meV (right).

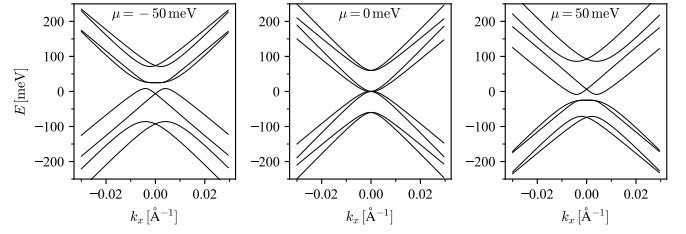


FIG. 12. Low-energy band structure for Kek-Y graphene ( $\Delta = 0.1$ ) with Rashba spin-orbit coupling ( $\lambda_\sigma = 60$  meV), including the term (E1) with different values of the parameter  $\mu$ .

In the limit of  $\frac{\lambda_\sigma}{\varepsilon_F} \ll 1$  we may approximate  $B_> \approx \frac{\varepsilon_F^2 + \lambda_\sigma^2}{2\hbar^2 v_\sigma^2}$ , yielding the magnetic field splitting

$$\delta B = \frac{2\lambda_\sigma^2}{\hbar^2 v_\sigma^2} \sqrt{\frac{c}{2e\hbar}} + O\left\{\left(\frac{\lambda_\sigma}{\varepsilon_F}\right)^2\right\}, \quad (\text{D5})$$

leading to Eq. (24).

#### APPENDIX E: IONIC POTENTIAL AND SECOND-NEAREST-NEIGHBOR CONTRIBUTIONS TO THE EFFECTIVE HAMILTONIAN FOR KEK-Y GRAPHENE WITH RSO COUPLING

For Kek-Y samples, the valley-sublattice term

$$\delta H = \frac{\mu}{2} (\tau_x \sigma_x s_0 + \tau_y \sigma_y s_0 - \tau_z \sigma_z s_0) \quad (\text{E1})$$

may appear due to two distinct mechanisms: the presence of a relative energy shift  $\mu_1$  between the Y-center and Y-end sites of the Kekulé pattern [21] and the presence of second-nearest-neighbor hopping energy  $t_2$ , giving [33]

$$\mu_2 = \frac{9\Delta^2 t_0^2 t_2^2}{t_0^2 - 9t_2^2}, \quad (\text{E2})$$

which together give  $\mu = \mu_1 + \mu_2$ . Whereas  $\mu_1$ , like  $\Delta$ , is an unknown,  $\mu_2$  can be estimated by considering theoretical values of  $t_2$ . For instance, Jung and MacDonald suggested [40]  $0.12|t_0| \leq |t_2| \leq 0.16|t_0|$ , such that for  $t_0 = 3.16$  eV and  $\Delta = 0.1$  we have  $39 \text{ meV} \leq |\mu_2| \leq 59 \text{ meV}$ . On the other hand, Kretinin *et al.* [41] provided a somewhat lower experimental estimate of  $|t_2| \approx 300$  meV based on measurements

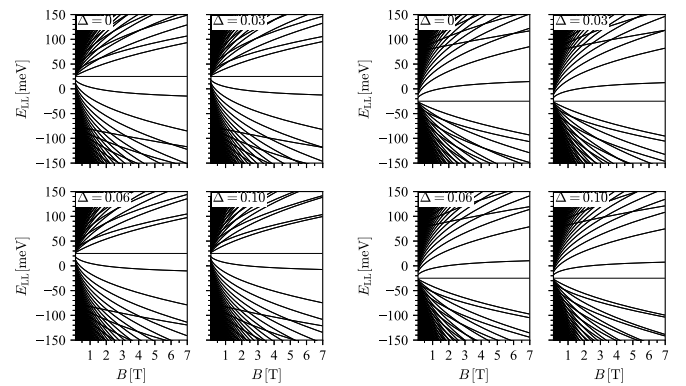


FIG. 13. Landau level spectra for Kek-Y graphene without Rashba spin-orbit coupling ( $\lambda_\sigma = 0$ ), including the term (E1) with  $\mu = -50$  meV (left) and  $\mu = 50$  meV (right).

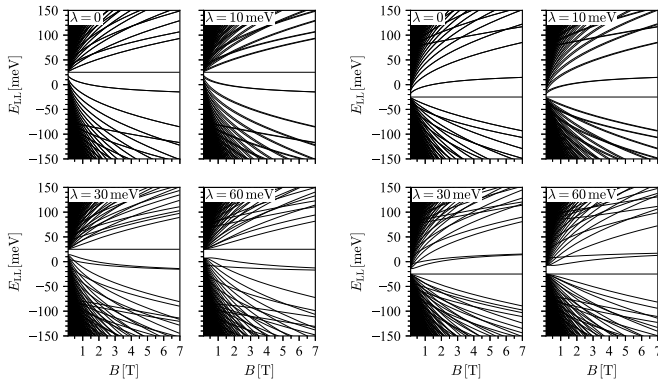


FIG. 14. Landau level spectra for pristine graphene ( $\Delta = 0$ ) with Rashba spin-orbit coupling, including the term (E1) with  $\mu = -50$  meV (left) and  $\mu = 50$  meV (right).

of the electron-hole asymmetry of graphene, yielding  $|\mu_2| \approx 29$  meV for  $\Delta = 0.1$ . Deacon *et al.* [42] made an even smaller estimate of  $|t_2| \approx 100$  meV based on Fermi velocity measurements from cyclotron resonance experiments, corresponding to  $|\mu_2| \approx 10$  meV. However, it is well understood that the graphene Fermi velocity and electron-hole asymmetry are directly related to  $|t_2|$  only in the single-particle approximation, whereas a many-body approach shows that these values are, in fact, strongly renormalized by electronic correlations [43].

Below, we show the effects of the term (E1) on the band and LL energies of Kek-Y graphene with RSO interaction. For the sake of concreteness, we take the upper limit  $|\mu| = 50$  meV and consider the possibility that  $\mu$  may be either negative or positive.

Figure 9 shows the well-documented case of Kek-Y graphene ( $\Delta = 0.1$ ) including the term (E1), showing the cases of  $\mu = -50$  and 50 meV, where the term  $\delta H$  changes the dispersion from two concentric Dirac cones meeting at the Fermi level into a single Dirac cone plus a gapped pair of parabolic bands. In the latter case, the Dirac point of the first pair of bands shifts above (below) the Fermi level for  $\mu < 0$  ( $\mu > 0$ ), with the bottom of the highest (top of the lowest) parabolic band being degenerate with the Dirac point.

Figure 10 shows the case of a pure ( $\Delta = 0$ ) Rashba spin-orbit coupling  $\lambda = 30$  meV, with  $\mu = -50$  and 50 meV. In this case,  $\delta H$  opens a gap and introduces a new two-valley structure to the valence (conduction) band for  $\mu < 0$  ( $\mu > 0$ ). The left panels in Fig. 11 show that both the band gap and the valley momentum increase with  $|\mu|$  and vanish at  $\mu = 0$ . Note that the conduction (valence) band edge for  $\mu < 0$  ( $\mu > 0$ ) is doubly degenerate and somewhat flat close to the  $\Gamma$  point

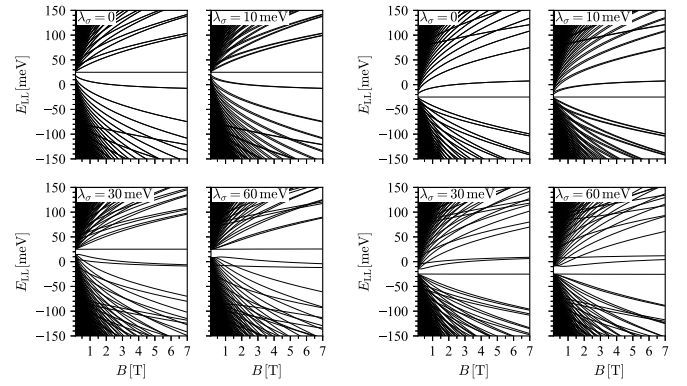


FIG. 15. Landau level spectra for Kek-Y graphene ( $\Delta \neq 0$ ) with Rashba spin-orbit coupling ( $\lambda_\sigma \neq 0$ ), including the term (E1) with  $\mu = -50$  meV (left) and  $\mu = 50$  meV (right).

of the Kekulé Brillouin zone and that the band structures for  $\mu > 0$  can be obtained from the ones for  $\mu < 0$  by mirroring the energies with respect to the Fermi level. Although these dispersion features occur at wave vectors  $k \sim 10^{-2} \text{ \AA}^{-1}$ , much smaller than the graphene Brillouin zone ( $\approx 3 \text{ \AA}^{-1}$ ) or the Kekulé Brillouin zone ( $\approx 1.7 \text{ \AA}^{-1}$ ), the salient feature at larger momenta is the splitting of the bands expected from only the Rashba spin-orbit coupling (shown in the middle panel of Fig. 10) by some tens of meV, although they exhibit the same Fermi velocities. This effect would be difficult to distinguish from the case of combined Rashba spin-orbit coupling and Kek-Y distortion (middle panel of Fig. 12), where that degeneracy is also broken.

A similar band gap and two-valley structure also appear in the combined case of Rashba spin-orbit and Kek-Y terms, as shown in Fig. 12. However, the right panels in Fig. 11 show that, in stark contrast to the case of  $\Delta = 0$ , for finite  $\Delta$  the valley momentum reaches a saturation value at  $\mu = 0$ , resulting in a sharp discontinuity as this value is crossed.

Finally, we discuss the LL spectra of the Kek-Y model modified with the term  $\delta H$ . Figures 13 and 14 show the cases of only Kek-Y and only Rashba spin-orbit coupling, respectively. The most salient feature of these spectra is, perhaps, the absence of zero-energy modes, although dispersionless (with respect to the magnetic field value  $B$ ) modes are observed above (below) the Fermi level for  $\mu < 0$  ( $\mu > 0$ ). These dispersionless modes correspond to the solution discussed in Eq. (B15) of Appendix B, with the exception that it now possesses an energy eigenvalue of  $-\mu/2$ . This is also the case for simultaneous Kek-Y and Rashba spin-orbit terms, as shown in Fig. 15.

- [1] E. Voloshina and Y. Dedkov, *Phys. Chem. Chem. Phys.* **14**, 13502 (2012).
- [2] P. A. Khomyakov, G. Giovannetti, P. C. Rusu, G. Brocks, J. van den Brink, and P. J. Kelly, *Phys. Rev. B* **79**, 195425 (2009).
- [3] G. Giovannetti, P. A. Khomyakov, G. Brocks, V. M. Karpan, J. van den Brink, and P. J. Kelly, *Phys. Rev. Lett.* **101**, 026803 (2008).
- [4] G. Song, M. Ranjbar, D. R. Daughton, and R. A. Kiehl, *Nano Lett.* **19**, 7112 (2019).

- [5] C. K. Safeer, J. Ingla-Aynés, F. Herling, J. H. Garcia, M. Vila, N. Ontoso, M. R. Calvo, S. Roche, L. E. Hueso, and F. Casanova, *Nano Lett.* **19**, 1074 (2019).
- [6] C. L. Kane and E. J. Mele, *Phys. Rev. Lett.* **95**, 226801 (2005).
- [7] A. Avsar, J. Y. Tan, T. Taychatanapat, J. Balakrishnan, G. Koon, Y. Yeo, J. Lahiri, A. Carvalho, A. S. Rodin, E. O'Farrell, G. Eda, A. H. Castro Neto, and B. Özyilmaz, *Nat. Commun.* **5**, 4875 (2014).

- [8] W. Han, R. K. Kawakami, M. Gmitra, and J. Fabian, *Nat. Nanotechnol.* **9**, 794 (2014).
- [9] B. Kandemir and A. Mogulkoc, *Solid State Commun.* **177**, 80 (2014).
- [10] Z. Lin, W. Qin, J. Zeng, W. Chen, P. Cui, J.-H. Cho, Z. Qiao, and Z. Zhang, *Nano Lett.* **17**, 4013 (2017).
- [11] D. Huertas-Hernando, F. Guinea, and A. Brataas, *Phys. Rev. B* **74**, 155426 (2006).
- [12] L. González-Árraga, F. Guinea, and P. San-Jose, *Phys. Rev. B* **97**, 165430 (2018).
- [13] A. López, L. Colmenárez, M. Peralta, F. Mireles, and E. Medina, *Phys. Rev. B* **99**, 085411 (2019).
- [14] C. Gutierrez, C.-J. Kim, L. Brown, T. Schiros, D. Nordlund, E. B. Lochocki, K. M. Shen, J. Park, and A. N. Pasupathy, *Nat. Phys.* **12**, 950 (2016).
- [15] C. Gutierrez, Ph.D. thesis, Columbia University, 2015.
- [16] D. Eom and J.-Y. Koo, *Nanoscale* **12**, 19604 (2020).
- [17] S.-Y. Li, Y. Zhang, L.-J. Yin, and L. He, *Phys. Rev. B* **100**, 085437 (2019).
- [18] C. Bao, H. Zhang, T. Zhang, X. Wu, L. Luo, S. Zhou, Q. Li, Y. Hou, W. Yao, L. Liu, P. Yu, J. Li, W. Duan, H. Yao, Y. Wang, and S. Zhou, *Phys. Rev. Lett.* **126**, 206804 (2021).
- [19] C. Bao, H. Zhang, X. Wu, S. Zhou, Q. Li, P. Yu, J. Li, W. Duan, and S. Zhou, *Phys. Rev. B* **105**, L161106 (2022).
- [20] A. Qu *et al.*, *Sci. Adv.* **8**, eabm5180 (2022).
- [21] O. V. Gamayun, V. P. Ostroukh, N. V. Gnezdilov, Í. Adagideli, and C. W. J. Beenakker, *New J. Phys.* **20**, 023016 (2018).
- [22] D. Marchenko, A. Varykhalov, M. Scholz, G. Bihlmayer, E. Rashba, A. Rybkin, A. Shikin, and O. Rader, *Nat. Commun.* **3**, 1232 (2012).
- [23] A. Varykhalov, J. Sánchez-Barriga, A. M. Shikin, C. Biswas, E. Vescovo, A. Rybkin, D. Marchenko, and O. Rader, *Phys. Rev. Lett.* **101**, 157601 (2008).
- [24] Y. S. Dedkov, M. Fonin, U. Rüdiger, and C. Laubschat, *Phys. Rev. Lett.* **100**, 107602 (2008).
- [25] O. Rader, A. Varykhalov, J. Sánchez-Barriga, D. Marchenko, A. Rybkin, and A. M. Shikin, *Phys. Rev. Lett.* **102**, 057602 (2009).
- [26] J. Sichau, M. Prada, T. Anlauf, T. J. Lyon, B. Bosnjak, L. Tiemann, and R. H. Blick, *Phys. Rev. Lett.* **122**, 046403 (2019).
- [27] S. Konschuh, M. Gmitra, and J. Fabian, *Phys. Rev. B* **82**, 245412 (2010).
- [28] Z. Tajkov, J. Koltai, J. Cserti, and L. Oroszlány, *Phys. Rev. B* **101**, 235146 (2020).
- [29] M. Peralta, E. Medina, and F. Mireles, *Phys. Rev. B* **99**, 195452 (2019).
- [30] B. Berche, F. Mireles, and E. Medina, *Condens. Matter Phys.* **20**, 13702 (2017).
- [31] J. M. Luttinger and W. Kohn, *Phys. Rev.* **97**, 869 (1955).
- [32] C. L. Kane and E. J. Mele, *Phys. Rev. Lett.* **95**, 146802 (2005).
- [33] E. Andrade, G. G. Naumis, and R. Carrillo-Bastos, *J. Phys.: Condens. Matter* **33**, 225301 (2021).
- [34] E. I. Rashba, *Phys. Rev. B* **79**, 161409(R) (2009).
- [35] We call a pair of in-plane vectors right-handed (left-handed) if their cross product points in the positive (negative)  $\hat{z}$  direction.
- [36] Y. Mohammadi and S. Bahrami, *Chin. Phys. B* **31**, 017305 (2022).
- [37] J. McClure, *Phys. Rev.* **104**, 666 (1956).
- [38] M. M. Otrokov, I. I. Klimovskikh, F. Calleja, A. M. Shikin, O. Vilkov, A. G. Rybkin, D. Estyunin, S. Muff, J. H. Dil, A. V. De Parga, R. Miranda, H. Ochoa, F. Guinea, J. I. Cerdá, E. V. Chulkov, and A. Arnau, *2D Mater.* **5**, 035029 (2018).
- [39] L. D. Landau and E. M. Lifshitz, *Quantum Mechanics: Non-relativistic Theory* (Elsevier, San Diego, 2013), Vol. 3.
- [40] J. Jung and A. H. MacDonald, *Phys. Rev. B* **87**, 195450 (2013).
- [41] A. Kretinin, G. L. Yu, R. Jalil, Y. Cao, F. Withers, A. Mishchenko, M. I. Katsnelson, K. S. Novoselov, A. K. Geim, and F. Guinea, *Phys. Rev. B* **88**, 165427 (2013).
- [42] R. S. Deacon, K.-C. Chuang, R. J. Nicholas, K. S. Novoselov, and A. K. Geim, *Phys. Rev. B* **76**, 081406(R) (2007).
- [43] N. Dale *et al.*, *npj Quantum Mater.* **7**, 9 (2022).